

www.acsami.org Research Article

Additive-Free and Support-Free 3D Printing of Thermosetting Polymers with Isotropic Mechanical Properties

Mohammadreza Mahmoudi, Scott R. Burlison, Salvador Moreno, and Majid Minary-Jolandan*



Cite This: https://dx.doi.org/10.1021/acsami.0c19608



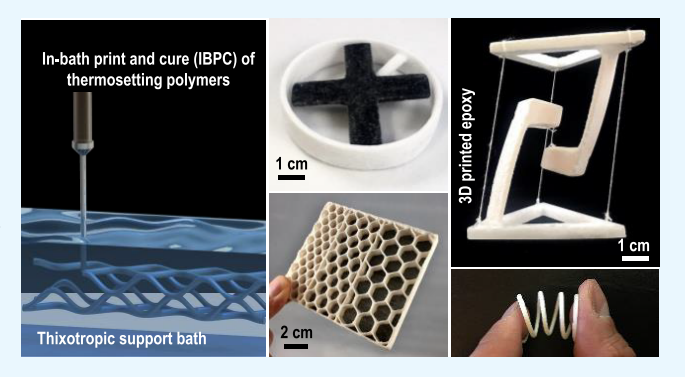
ACCESS

III Metrics & More



Supporting Information

ABSTRACT: The democratization of thermoplastic 3D printing is rooted in the ease of processing enabled by economical melting and shaping. Thermosetting polymers, on the other hand, have not enjoyed this advantage given that thermosetting resins cannot hold their shape without cross-linking or excessive fillers, and once cross-linked, they cannot be extruded for printing. Due to this formidable challenge, thus far, 3D printing of thermosetting polymers has been limited to the photopolymerization of specialized photosensitive resins or extrusion of resins loaded with large fractions (as high as 20 wt %) of rheology modifiers. Here, we report a rheology-modifier- and photoinitiator-free process for the 3D printing of a pure commercial epoxy polymer, without any resin modification and using a conventional 3D



printer. A low-cost non-Newtonian support material that switches between solid—fluid states under a nozzle shear stress enables the printing of complex 3D structures and the subsequent and "one-step" curing. Our results show that the one-step curing eliminates the often-compromised interlayer adhesion common in layer-by-layer 3D printing processes and results in unprecedented isotropic mechanical properties (strength, elastic modulus, tensile toughness, and strain to failure). This in-bath print and cure (IBPC) 3D printing process for thermosetting polymers is low-cost, scalable, high-speed (nozzle speeds exceeding 720 cm/min), and high-resolution (down to 220 μ m filament size). We demonstrate potential applications for hobbyists, structural and aerospace components, and fiber-reinforced composites, among others.

KEYWORDS: 3D printing of polymers, thermosetting polymers, additive manufacturing, mechanical properties, epoxy

■ INTRODUCTION

The three-dimensional printing (3D printing) of polymeric materials has disrupted how we build complex and customized structures. 1-9 The ease in the processing of thermoplastic polymers, which involves melting and depositing molten plastics, has resulted in widely available low-cost 3D printers for the general public. However, thermoplastics suffer from several disadvantages: the temperature gradient between the previous layer and the deposited one results in thermal gradient and residual stress, which leads to warping, and the interlayer interface in thermoplastics relies on the partial diffusion of polymer chains, which results in weak interfaces. On the other hand, thermosetting (TS) polymers do not require thermal energy input to process and can be processed at room temperature (or slightly elevated temperature), eliminating the thermal gradient issue; the interlayer interface in thermosetting polymers is based on cross-linking, which results in stronger interfaces. In addition, TS polymers are generally cheaper than thermoplastics. Furthermore, the superior thermal stability and mechanical properties and excellent chemical resistance make TS polymers and their composites desirable for aerospace, energy, and automotive applications.^{10,11} Except for highly reactive thermosets,^{10,12} the majority of TS polymers require several hours of high-temperature curing, which is not compatible with the requirement of 3D printing processes that the material should hold its shape for successive layers to build up. Unless cross-linked, TS polymers generally cannot retain their shape, and once cross-linked, they are not extrudable. This remains a formidable challenge for the 3D printing of TS polymers. So far, 3D printing of TS polymers has been mainly limited to photocurable processes, which require specialized resins.^{1,4,8,13–15} One solution to mediate this problem has been to use rheology modifiers or thickeners such as nanoclay and silica nanoparticles to obtain the required shear-thinning behavior for the ink for the direct ink writing (DIW) process.^{11,16,17} However, the need for a substantial weight

Received: November 3, 2020 Accepted: January 12, 2021



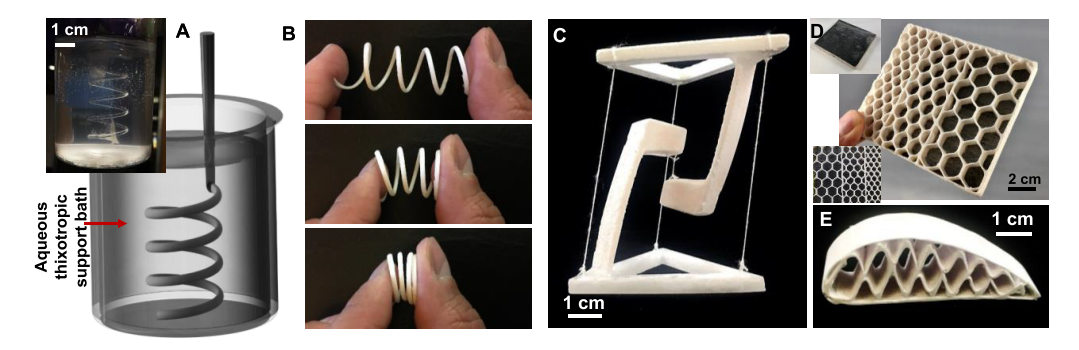


Figure 1. The IBPC thermoset 3D printing process and examples of the 3D-printed structures. (a) The schematic illustration and an image show the printing of a helix inside a thixotropic bath. (b) The 3D-printed epoxy helix shows excellent deformability. (c–e) Images of a 3D-printed tensegrity table, a gradient honeycomb, and an airfoil.

fraction (up to 20 wt %) of rheology modifiers is still a limiting factor. So far, 3D printing of pure commercial TS polymers without rheology modifiers or photoinitiators has not been achieved.

We report a rheology-modifier- and photoinitiator-free approach to 3D printing of TS polymers, which is capable of the continuous and high-speed printing of off-the-shelf commercial TS polymers using conventional extrusion printers (Figure S1, Movie S1). The process is low-cost and can print objects of several centimeters in size in a few minutes. Moreover, the cure-after-print (as opposed to layer-by-layer cross-linking) results in strong interlayers and isotropic mechanical properties (independent of the print direction). Specifically, strength, elastic modulus, strain to failure, and tensile toughness were found to be independent from the print direction. The presence of the sacrificial support bath also eliminates the need to print and remove support structures.

■ RESULTS AND DISCUSSION

The printer operates on the principle of direct extrusion of a TS resin into a non-Newtonian fluid bath (Figure S2). Lewis and co-workers reported the omnidirectional printing of 3D microvascular networks by printing fugitive ink filaments within a photocurable gel reservoir, which physically supports the patterned features. 18 This process was extended to bioprinting applications in which a bath serves as a temporary and biocompatible support to print complex biological samples containing cells and hydrogels. ^{19,20} Hinton et al. reported 3D printing of hydrophobic polydimethylsiloxane (PDMS) elastomer in a hydrophilic carbopol gel via freeform reversible embedding (FRE).²¹ This study demonstrated that hydrophobic polymers with low viscosity and long cure times can be 3D printed using a hydrophilic support. O'Bryan et al. reported a method to make micro-organogels swollen in mineral oil using block copolymer self-assembly to enable 3D printing of oil-based materials such as silicone. The results showed that the rheological properties of this micro-organogel material are tunable, leveraging the jamming transition, which facilitates its use in 3D printing of silicone structures.²² Afghah et al. used a composite pluronic-nanoclay support bath, which resulted in a shear-thinning composite support bath with fast self-recovery behavior, for the bioprinting of cell-laden alginate-based hydrogels.²³

We build on these concepts by leveraging the two-step curing of a pure epoxy ink (epoxy resin and curing agent) extruded inside a thixotropic (time-dependent shear thinning) support bath. The thixotropic bath shows time-dependent microstructure collapse and buildup in the presence and absence of a moving nozzle, respectively. The microstructure collapse allows for the extrusion of the epoxy ink, and the buildup physically supports the printed ink to print complex 3D structures in a layer-by-layer or omnidirectional fashion. Once the printing process is over, the thermosetting polymer is first "partially cured" inside the bath in a room environment for 12–24 h, "at once". This one-step partial curing eliminates the weak interlayer interface often encountered in layer-by-layer processes such as FDM (fused deposition modeling). We term this process in-bath print and cure (IBPC) for 3D printing of thermosetting polymers.

A thixotropic fluid can switch between a solid behavior and fluid behavior under shear stress (mayonnaise and shaving cream have this property). This property can be observed as the bath can hold its shape when kept upside down, while if it is vigorously shaken, it will flow. When the nozzle moves in a thixotropic fluid, under the nozzle shear stress, the bath fluidizes in the nozzle vicinity. The bath returns to a solid behavior behind the nozzle track. When the low-viscosity epoxy is extruded from the nozzle tip, the printed geometry is maintained stable once the thixotropic fluid returns to its solid behavior. Once printing is finished, the printed epoxy is first partially cured (cross-linked). The partially cross-linked epoxy is retrieved from the bath and fully cured in an oven.

During this partial cure, the cross-link density in the epoxy increases and results in a structure that can be pulled out of the bath and subsequently fully cured in an oven at higher temperatures. Thermal analysis shows that the partially cured epoxy shows a glass transition temperature ($T_{\rm g}$), albeit at a much lower temperature compared to the fully cured epoxy, followed by residual curing at higher temperatures. The presence of detectable $T_{\rm g}$ shows that room temperature curing generates enough cross-linking density in the material such that it can maintain its shape during pullout from the bath, as well as during several hours of subsequent full cure. Since the partial curing occurs in a room environment, we used an aqueous thixotropic bath (Laponite in DI water). Hence, the partial curing occurs inside the water, which may also facilitate the heat dissipation during the exothermic curing process.

The IBPC process enables 3D printing of complex 3D structures using "pure" epoxy without any need for rheology modifiers that are required in the direct ink writing (DIW) process¹¹ or the modification of the resin with specialized photoinitiators for photocurable processes.^{1,4} Because the bath functions as the sacrificial support, there is no need to print support structures even for complex geometries. As an

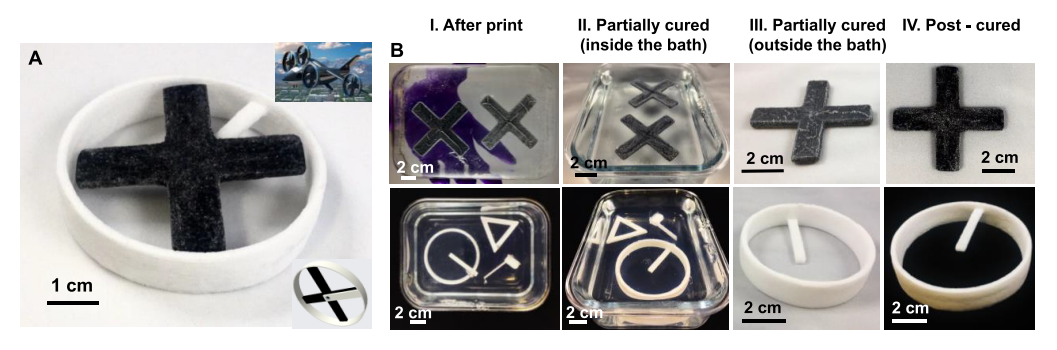


Figure 2. The steps in 3D printing carbon fiber reinforced epoxy composite. (a) An image of the 3D-printed ducted fan. The propeller is printed using chopped carbon fiber reinforced epoxy. The insets show the corresponding computer image and an air taxi with four ducted fans. (b) The steps in the IBPC process: print and partially cure inside the thixotropic bath and post-cure inside an oven. The dark-colored material in the images is the 3D-printed carbon fiber reinforced epoxy.

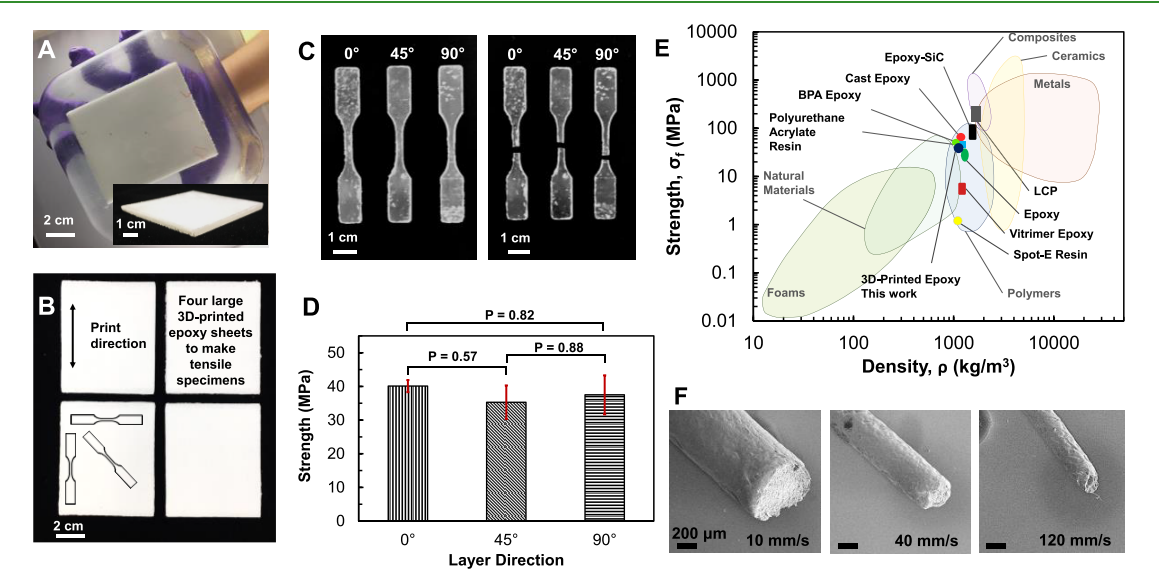


Figure 3. Isotropic mechanical properties of the printed structures. (a) An image of a 3D-printed epoxy sheet for the tensile test inside and outside the bath. (b) Tensile test specimens were punched out from the printed sheets using an ASTM standard die in different orientations with respect to the print direction. (c) Photos of the dogbone specimens before and after the tensile test. (d) Strength for samples with different printing layer directions. (e) An Ashby plot for strength vs density comparing the properties of the printed epoxy in this work with the literature (details are provided in the Supporting Information). (f) The SEM images of the filaments printed in three speeds (10, 40, and 120 mm/s).

example, we printed a helical spring with a wire diameter of 1.5 mm and a mean diameter of 20 mm using omnidirectional printing inside the bath (Figure 1a). The spring is deformable and fully elastic for many cycles given the absence of any additives in the ink (Figure 1b). We also demonstrated printing of a tensegrity table (Figure 1c), a honeycomb structure with a gradient lattice (Figure 1d, Figure S3, Movies S2–S3), equilateral triangles (Figure S4), and an airfoil (Figure 1e). The tensegrity structure is supported by four threads in which the cotton threads are in tension, while the discontinuous support beams are in compression.

In a sandwich panel, the core transfers the force to the load-carrying skin. The gradient lattice structure generated by 3D printing will allow for the optimization of the lattice size based on the load profile, for example, in beam structures. A carbon fiber (5 wt %) reinforced epoxy skin was printed on one side of the panel (Figure S3, Movie S4). Given their superior mechanical properties, thermosetting polymers may be used for urban air mobility applications. As a proof of concept, we printed a small-scale ducted fan, Figure 2a (of an air taxi, inset), in which the propeller (dark color) is a carbon fiber reinforced epoxy (Figure S5). To assess whether the shear

stress in the nozzle results in carbon fiber alignment, we acquired SEM images from freeze-fractured carbon fiber reinforced filaments. The SEM images were acquired parallel to the cross section of the filament (Figure S5c-e). It can be observed from the SEM images that the fibers are partially aligned along the filament axis. We performed image analysis to quantify the angle of the carbon fibers with respect to the filament axis, and the results are shown in Figure S5f.

All these structures with several centimeters in size were printed in several minutes, for example, the air foil and the gradient honeycomb took ~3 and ~13 min, respectively (Table S1). Different stages of the IBPC process are shown in Figure 2b, which shows parts (i) after printing inside the bath, (ii) after partial curing in the bath and (iii) out of the bath, and finally (iv) after post-curing in an oven. The printed parts are stable and maintain their geometry throughout the process for hours even in the uncured phase inside the bath.

Most often, in 3D-printed materials, the interlayer interfaces are the weakest links, which often arise from layer-by-layer deposition and curing. For these materials, the mechanical properties are anisotropic, with properties being better along the print direction than the transverse direction, often by

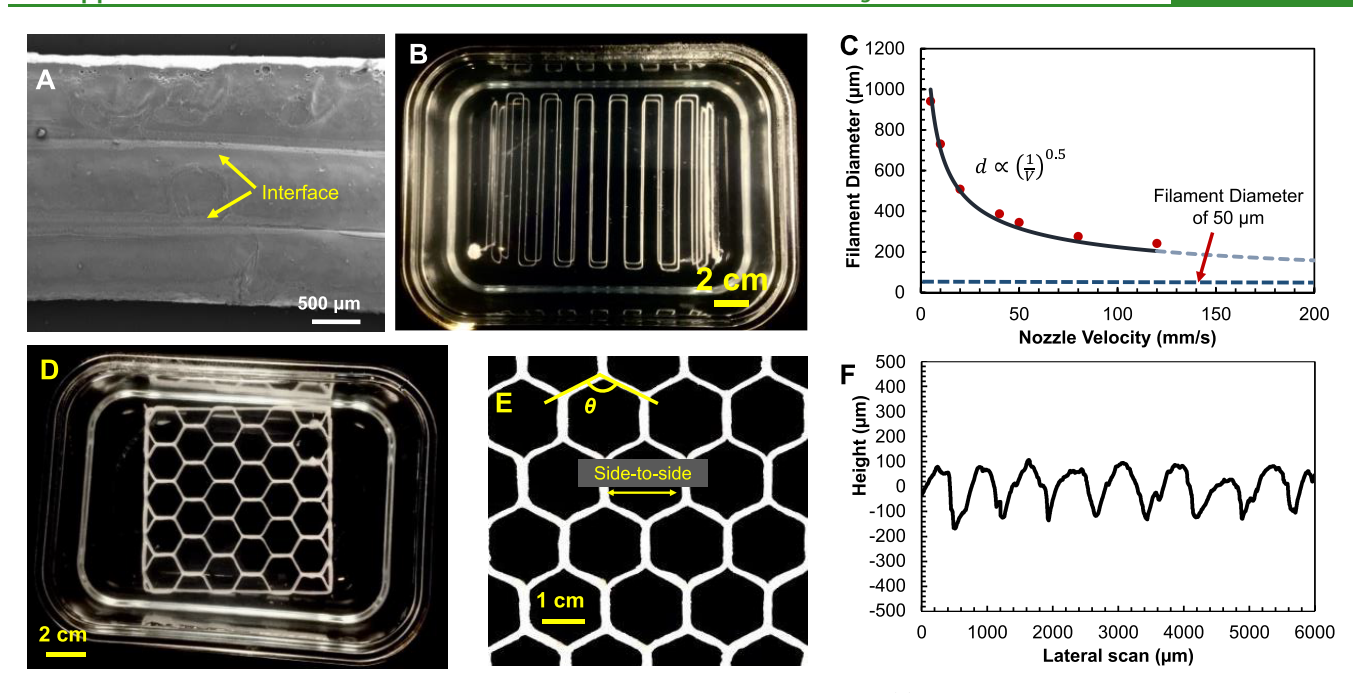


Figure 4. High-quality interlayer interface, print fidelity, and print diameter vs nozzle speed. (a) An SEM image shows the interlayer interface between three printed epoxy layers; nearly perfect bonding in the interface is observed. (b) Filaments printed with different nozzle speed. (c) The printed filament diameter vs nozzle speed. The solid line shows a trend line based on $\propto \sqrt{\frac{1}{V}}$. The horizontal dashed line shows the filament diameter of 50 μ m, which is associated with the onset of the Rayleigh instability, corresponding to the nozzle speed of \sim 2000 mm/s. (d) A photo of a printed honeycomb inside the support bath. (e) A zoomed-in view after post-curing used for print fidelity (length and angle) analysis. (f) A profilometer height profile acquired from the surface of a sample printed with a nozzle speed of 50 mm/s.

several times. 11,17,24 Recently, the HARP process has been introduced by Mirkin and co-workers for 3D printing of photocurable resins, in which the continuous printing enabled by a mobile liquid interface resulted in isotropic mechanical properties regardless of the print direction. To determine whether the IBPC process results in an isotropic material, we performed a tensile test based on the ASTM standard. For these experiments, we printed large sheets of epoxy, $\sim 10 \times 8$ cm (Figure 3a, Movie S5, Figure S19). Tensile specimens were punched out using an ASTM D638 Type V cutting die in different orientations (0, 45, and 90°) relative to the printing direction (Figure 3b). The surface finish depends on several factors including the nozzle speed and also the interfacial tension between the bath and the epoxy and the yield stress of the bath. Since the nozzle velocity affects the filament diameter, it would also affect the surface finish of the printed sheets. Samples printed at higher speeds should have smoother surfaces since individual filaments that form the surface will have a smaller diameter. For mechanical measurements, we polished the surface of the samples. The high surface tension tends to minimize the surface area. This seems to be the reason for having a relatively smooth surface for the printed sheets.

The specimens showed a similar fractured pattern (Figure 3c). The results showed that the specimens have isotropic mechanical properties indicated by insignificant Tukey's HSD (honest significance difference) test (Figure 3d, Figure S6, and Tables S2–S3). The strength of the tensile specimens at printing directions of 0, 45, and 90° was 40.1 ± 1.8 , 35.3 ± 5 , and 37.5 ± 5.8 MPa, respectively. Generally, additive manufacturing processes produce objects that have inferior mechanical properties compared to the conventional manufacturing processes. This can be attributed to several factors depending on the process and material type. These factors

include the formation of voids during printing, cold junction between interfaces, and poor surface finish, among others. In the case of the process presented in this work, the bath (water) may also affect the mechanical properties. To ensure that the underlying material strength was measured, we slightly polished the surface of the tensile sheets. To visualize the internal structure of the printed specimens, we acquired micro-CT images. Figure S20 shows a 3D micro-CT image of a broken tensile specimen. The void diameter distribution histogram shows the size of the voids detected within the machine resolution (> \sim 3 μ m). We calculated the void volume fraction by dividing the void volume by the total volume. The void volume fraction was calculated to be less than ~0.1%. Moreover, we measured the density of the printed objects using the Archimedes method. The obtained density (\sim 1.15 g/ cm³) was in good agreement with the density of Epon epoxy (\sim 1.2 g/cm³). From the micro-CT and density measurements, we conclude that the printed objects are nominally solid with a very low void volume fraction. In other words, the printed material is solid with no apparent porosity (Figure S7). We believe that the combination of surface defects and bath effect (effect of water during curing) may have resulted in lower mechanical properties compared to cast epoxy. This point deserves more investigation to fully understand the bath effect in this process.

Figure 3e shows an Ashby plot for strength vs density comparing the properties of the 3D-printed epoxy in this work with the literature (references are provided in Table S4). Isotropic mechanical properties are often an indication of strong interlayer interfaces. We examined the interface between the printed layers using scanning electron microscopy (SEM). The SEM results show that the interlayer interfaces are fully fused with each other (Figure 4a), which indicate that the

presence of the bath does not affect the interface, and consecutive printed layers form strong chemical bonds after full cure.

To evaluate the printing resolution of the IBPC process, we printed single filaments under a constant flow rate while increasing the nozzle speed (V). The nozzle speed was increased from 5 up to 120 mm/s (the speed limit of the printer) (Figure 4b and Figure S8). We measured the filaments' diameters using SEM (Figure 3f, Figure S9, and Table S5). The results show that filaments are circular, and the filament diameter decreases from ~945 to ~220 µm when the nozzle speed increases from 5 to 120 mm/s. The nozzle diameter to print these filaments was \sim 840 μ m. Hence, with the same nozzle, various filament diameters can be printed by changing the nozzle speed. We found that the filament diameter (d) vs the nozzle speed estimated from volumetric print rate $Q\left(Q \sim \frac{\pi d^2}{4}V\right)$ follows a similar trend $\left(d \propto \sqrt{\frac{1}{V}}\right)$ to the measured filament diameter (Figure 4c and Figure S10), albeit the measured diameters are consistently smaller than the theoretical estimate. This shows that the volumetric print rate does not solely define the print diameter.

One would expect that by further increasing the nozzle speed, smaller features can be obtained. This trend can be continued up to the point at which the interfacial tension between the bath and the thermosetting polymer breaks up the printed filament to individual droplets, a phenomenon identified as the Plateau-Rayleigh instability, according to which liquid jets break into droplets to minimize their surface area (energy).²⁵ The yield stress of the bath (σ_y , which was measured to be ~76 Pa) is the opposing force, while the interfacial tension $(\gamma_{bath - polymer})$ is the driving force for such instability. The minimum stable feature size can be estimated to be $\frac{\gamma_{\rm bath-polymer}}{\sigma_{\rm y}}$. The interfacial tension of the epoxy and the stable feature size for the epoxy and the aqueous bath system is estimated to be $\sim 50 \mu m$. By extrapolating the filament diameter vs nozzle speed, an upper limit for nozzle speed is estimated to be $\sim 2000 \text{ mm/s}$ (Figure 4c), above which the printed filament will break up to individual droplets. Such phenomenon has been recently explored for printing droplets inside a yield stress bath.²⁵

The IBPC process is capable of printing with high fidelity. As a demonstration, we measured the average angle (119.6 \pm 2.8°) and the side-to-side length (15.9 \pm 0.12 mm) of a honeycomb structure and compared them to the CAD model input to the printer (120° and 16 mm, respectively) (Figure 4d,e). The surface ridges on the printed part depend on the filament diameter and hence the nozzle speed (Figure 4c). For a nozzle speed of 50 mm/s and a flow rate of 0.8 mL/min, the profilometer shows surface ridges with a peak-to-valley of approximately 200 $\mu \rm m$ and an average peak-to-peak of approximately 720 $\mu \rm m$ (Figure 4f). Faster nozzle speeds will result in thinner filaments and, hence, smoother surface and better resolution. If the goal is to increase the volumetric print rate, variable speed pumps may be needed to increase the flow rate (Q) while the nozzle speed increases.

As the nozzle moves in the bath, it creates a crevasse behind it. As an analogy, consider cutting a gel with a knife. As opposed to conventional gels (which are often brittle), a thixotropic material will "heal" and close the crevasse after a

certain time. The driving force for the closure is the hydrostatic pressure, while the viscous force $(v\eta/d)$ of the bath is the resisting force, in which v and d are the nozzle velocity and diameter, respectively, and η is the bath viscosity. The closure of the crevasse behind the nozzle will prevent the reflow of the dispensed polymer into this space. The hydrostatic pressure (ρgh) depends on the depth (h) in which the material is being printed, where ρ is the bath density. The printing depth in this study was in the range of $\sim 2-6$ cm. To evaluate the viscous force, we measured the bath viscosity as a function of shear rate, $\dot{\gamma} \approx \frac{V}{d}$ (Figure 5a). The results show that the bath

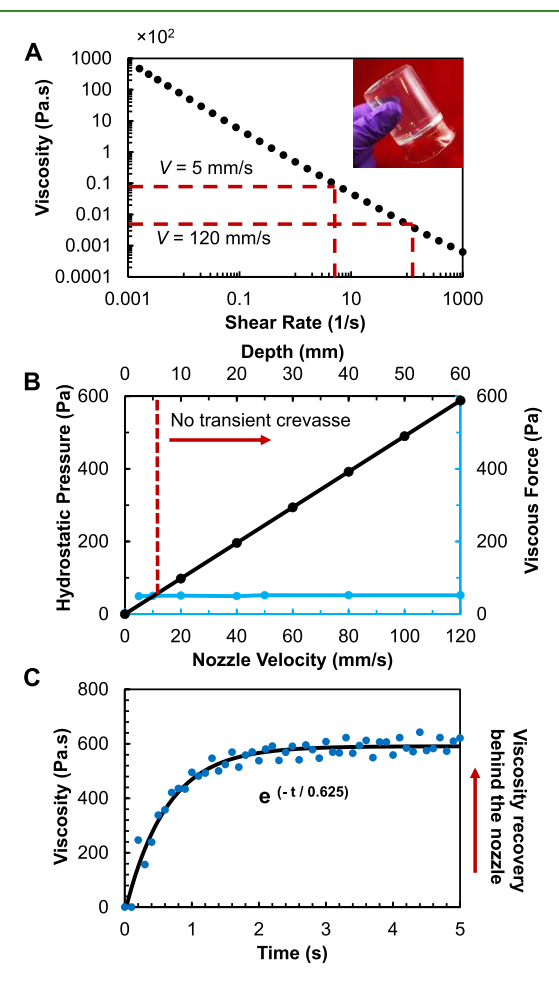


Figure 5. The rheological properties of the thixotropic support bath and viscous force have crucial effects on the process outcomes. (a) The viscosity vs shear rate for the thixotropic support bath. (b) The hydrostatic pressure vs bath depth and the viscous force vs nozzle velocity. The viscous force is nearly constant. (c) The buildup of the bath viscosity vs time extracted from the 3ITT. The solid line is an exponential fit.

viscosity nearly linearly drops vs the shear rate, and as a result, the viscous force remains approximately constant (Figure 5b and Table S6). For these experimental conditions, we calculated that the printing depth should be more than 5 mm to ensure the closure of the crevasse behind the nozzle (Figure Sb). We could observe that, in a shallow depth (<~5 mm), nozzle track marks were left on the gel, while for a larger depth, no track mark behind the nozzle could be observed in the bath (Figure S13 and Movie S6).

ACS Applied Materials & Interfaces

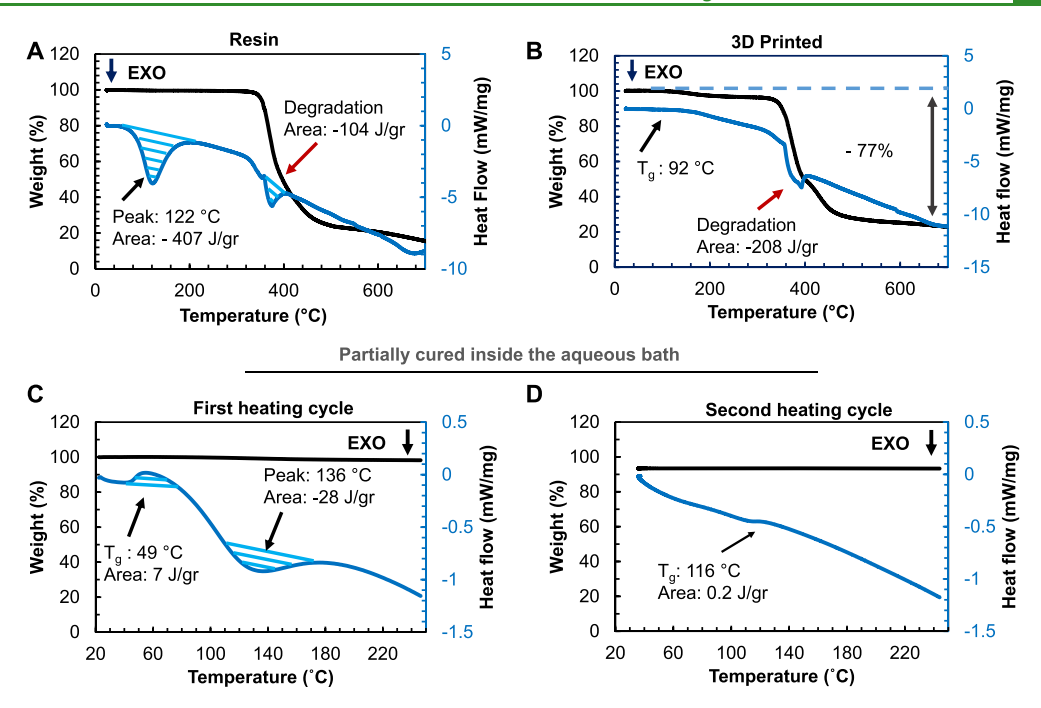


Figure 6. Differential scanning calorimetry (DSC) and thermal gravimetry analysis (TGA) to analyze the thermally induced chemical reactions during partial cure and full cure. (a and b) DSC/TGA responses for the resin and the 3D-printed epoxy, respectively. (c and d) DSC/TGA responses of the partially cured epoxy inside the aqueous bath for the first and second cycles, respectively.

The Reynolds numbers $(Re = \frac{\rho \cdot V \cdot d}{\eta})$ of 10–15 are often associated with the onset of turbulent flow around a moving cylinder in a fluid.²⁷ For the epoxy flowing through the nozzle, we calculated the Re = 0.005, which is well within the laminar flow range. We calculated that the flow speed in the nozzle should increase to ~23.8 m/s for the onset of turbulent flow (Re = 10), which corresponds to a flow rate of over \sim 710 mL/ min. The other relevant Re number is associated with the moving nozzle in the bath. Since the viscosity and nozzle speed have an inverse relationship, the Re number increases nonlinearly with the nozzle speed (Figure S12). The calculated Re number shows that at a nozzle speed of ~750 mm/s, the onset of turbulent flow in the bath resulting in a recirculating flow and unstable printing can be expected. We note that the bath Re number was calculated from the experimentally measured bath viscosity vs the nozzle velocity (Table S6).

The shear strain rate varies from \sim 4 to \sim 100 s⁻¹ for the nozzle speed of 5-120 mm/s. This corresponds to a viscosity in the range of ~12 Pa·s down to ~0.5 Pa·s. As a comparison, the viscosity of the epoxy used in this work was ~2.2 Pa·s (21.9 P) (Figure S21). We used a nozzle speed in the range of \sim 40– 50 mm/s for most of the printed structures, which corresponds to a shear strain rate of 30-40 s⁻¹, and a bath viscosity of ~1.25-1.5 Pa·s. To investigate the recovery of the bath viscosity behind the nozzle, we performed the 3ITT (the threeinterval thixotropic test), in which the bath was subjected to step strain rates between 0.1 and $\sim 100 \text{ s}^{-1}$ (Figure S14). The viscosity recovery vs time when the shear rate changes from \sim 100 to \sim 0.1 s⁻¹ is shown in Figure 5c. The data are fit by an exponential function with a thixotropic time constant of τ = 0.625 s. In the wake of the nozzle, the bath viscosity quickly recovers the majority of its static viscosity (in a short time (<1 s), which is enough to maintain the geometry of the printed polymer). Additionally, this fast recovery time allows for the nozzle to return back to the same location to continue printing the subsequent layers. Laponite in water forms a threedimensional network that results in the observed timedependent shear-thinning/thickening behavior (thixotropic). This thixotropy is the result of the breakup and buildup of the 3D microstructure of Laponite in water. There is a time constant associated with this breakup and buildup that results in the observed time-dependent behavior.

During epoxy cross-linking, the epoxide group in epoxy resin reacts with the curing agent to form a highly cross-linked threedimensional network. To investigate the thermally induced chemical reactions during the process, we performed simultaneous differential scanning calorimetry (DSC) and thermogravimetric analysis (TGA) measurements under flowing nitrogen. The exothermic peak of epoxy resin curing (cross-linking) has a peak at ~122 °C, with an onset and endpoint of 86 and 168 °C (Figure 6a). The second exothermic peak at ~375 °C, which is accompanied by a large drop in mass in the TGA response, is associated with degradation (thermal decomposition). The 3D-printed epoxy shows a $T_{\rm g}$ of ~92 °C. The $T_{\rm g}$ has an onset and endpoint at 77 and 107 °C, respectively (Figure 6b). For the cast epoxy, the T_{σ} onset and endpoint are 87 and 136 °C, respectively (Figure S15). Based on the TGA response, the cast and 3D-printed epoxy show a similar degradation (decomposition) response (Figure S16).

In conventional processes including casting, the epoxy resin is cured in air or an inert gas environment. In this process, however, we performed the initial partial cure inside the aqueous bath at room temperature followed by the full cure out of the bath in an oven at an elevated temperature (85 °C). To further evaluate the thermal behavior of the partially cured epoxy inside the aqueous bath, we performed two heating cycles on this sample up to 250 °C (well below the decomposition temperature). In the first heating cycle (Figure 6c), we observed an endothermic peak for $T_{\rm g}$ at ~49 °C, with an onset and endpoint of 41 and 55 °C, respectively. The

second peak is exothermic with a peak at 136 °C and an onset and endpoint of 102 and 177 °C, respectively. This peak is associated with residual curing. In the second heating cycle (Figure 6d), the $T_{\rm g}$ was detected at ~116 °C. No noticeable drop in weight was detected based on the TGA data for either cycle. The results reveal that the initial partial cure at room temperature inside the bath results in a low cross-link density, and hence, the detected $T_{\rm g}$ for the first cycle is much lower than the cast epoxy. The residual cure in the first cycle results in a higher cross-link density, and consequently, the $T_{\rm g}$ increases to a value close to the cast epoxy. Only 0.5 wt % of water evaporation was measured for the partially cured epoxy, an indication that the residual water inside the partially cured epoxy was minimal (Figure S17).

To compare the chemical composition of the printed epoxy vs the control cast epoxy, we acquired EDS (energy-dispersive X-ray spectroscopy) spectra from both the surface and the cross section of the printed epoxy. The spectra and the material composition matched the ones of the cast epoxy (Figure S18, Table S7), and no detectable traces of the Laponite were found on the printed samples.

For 3D printing of epoxy in the literature, rheology modifiers are used. In our case, the use of bath eliminates using any rheology modifiers. This is very important for achieving isotropic mechanical properties. This article also reports on the details of a two-step curing (partial curing in the bath and complete curing outside of the bath) with detailed thermal analysis. 3D printing of epoxy needs a careful choice of support bath. For the PDMS and hydrogels, often a low-yieldstress (~<10 Pa) bath is used. According to the Rayleigh instability, the minimum printable feature size depends on the ratio of the interfacial tension and the yield stress of the bath. In our preliminary experiments, we observed that for support bath with a low yield stress (mineral-oil-based gel), the printed parts (epoxy) broke up unless the diameter of a single filament was as high as \sim 3 mm. Therefore, we designed a support bath with a high yield stress (~76 Pa) to be able to achieve a better resolution. We also intended to have a transparent bath for the in situ monitoring of the process for subsequent research underway in our group.

The support bath is designed in a way that it prevents rise or sinks of the printed part as we have seen that the parts and filaments were in place during the printing and room temperature curing. The case of single-filament printing differs from when filling a space. In the latter case, the bottom side and one side of the extruded filament are in contact with the previously printed epoxy, while the top surface and the other side surface are in touch with the bath. This top surface and the side surface come into contact with the next filaments and next layers. Since the epoxy does not cure, we believe that the interdiffusion between printed layers overall results in all sides of a filament within a space-fill print to have similar dimensions and curvature. This effect, however, will show up in the uppermost top and bottom and side layers, which essentially form the sample surface. The time-dependent shear thinning and thickening (thixotropy) may play a role in the resolution and also surface finish of the sample. If the bath recovery time is too long, the epoxy may spread into the bath and compromise the resolution. On the other hand, the recovery time may also smoothen the surface, as the adjacent lines have enough time to merge before the bath fully recovers. There may be a trade-off between the resolution and surface

smoothness of the printed object depending on the recovery time, and this deserves a full study.

Although our focus in this work has been on the effect of speed on the printing performance, it is also important to discuss the role of nozzle diameter in the printing performance. The viscous force $(v\eta/d)$ of the bath, in which η is the bath viscosity, which is the resisting force to crevasse closure, depends on the nozzle velocity (v) and nozzle diameter (d). By increasing the nozzle diameter, the viscous force would decrease. In addition, the bath viscosity is a function of the shear rate, $\dot{\gamma} \approx \frac{V}{d}$. By increasing the nozzle speed, the shear rate would reduce, which corresponds to a higher bath viscosity. As a result, the viscous force remains approximately constant, as shown in Figure 5b. Therefore, theoretically, the diameter does not have a direct effect on the viscous force. This needs to be experimentally verified in future work. The nozzle diameter can also affect the volumetric flow rate (print rate). For a fixed flow rate, the larger the diameter, the smaller the nozzle speed required to achieve the same filament diameter.

CONCLUSIONS

Overall, the IBPC process overcomes several limitations facing the 3D printing of thermosetting polymers, namely, the need for rheology modifiers (for direct extrusion) or specialized chemistries (for photocurable processes), the weak interlayer interface in layer-by-layer curing, and the need to print and remove support structures. Several challenges remain: new support baths should be developed through engineering the bath microstructure and rheological properties that allow for even finer structures and faster printing speeds to be achieved; methods for incorporation of continuous fibers in the printed material can further expand applications to load-bearing structures; and new resins and hardener chemistries can be developed for a faster cure and higher overall throughput.

■ EXPERIMENTAL SECTION

Epoxy Preparation. Epoxy solution was prepared by mixing Epon Resin 862 (Hexion) and Epikure curing agent 3234 (Hexion) at a 100:16 weight percent ratio. All chemicals were used as received. The solution was mixed using a vortex mixer for 2 min followed by degassing under a vacuum for 5 min. Epon Resin 862 is a low-viscosity liquid epoxy resin, which is manufactured from epichlor-ohydrin and bisphenol F. This resin contains no diluents or modifiers. Triethylenetetramine (TETA) is an organic compound with the formula $[CH_2NHCH_2CH_2NH_2]_2$. The reactivity and applications of TETA are similar to the related polyamines ethylenediamine and diethylenediamine. It can be used as a cross-linker or hardener in epoxy. TETA is available as Epikure curing agent 3234, which is an unmodified aliphatic amine.

Carbon Fiber/Epoxy Composite Preparation. Short carbon fibers (Zoltek Corporation) were added to the epoxy at a 5:100 weight percent ratio. The average length and diameter of the carbon fibers were ~ 100 and $7.2~\mu m$, respectively. The solution was mixed for 2 min using a vortex mixer. The epoxy/CF were degassed under a vacuum for 5 min. Higher loadings of carbon fibers are only possible when fibers are aligned or the aspect ratio of the fibers is too small. In our process, the fibers aligned partially through the long small-diameter nozzle by the syringe pump pressure (Figure S5). A drastic increase in the fiber volume ratio will result in the nozzle clogging. We increased the fiber/polymer ratio to find the threshold such that the epoxy/CF mix was easily flowable.

Support Bath Preparation. The support bath was prepared by mixing 4 wt % Laponite RD (BYK Additives and Instruments) in 96 wt % DI water at room temperature. The Laponite RD was added to

DI water while a magnetic stirrer was used at 1200 rpm until all particles dispersed into DI water, and it turned to a colorless and translucent colloidal dispersion. Subsequently, it sat for approximately 2 h at room temperature to complete the hydration process for the formation of the thixotropic fluid.

3D Printing. Printing was performed using a Delta-type 3D printer designed and built at UT Dallas. The epoxy resin was loaded into a 20 mL syringe and injected by an NE-300 Just Infusion syringe pump. A needle with an inner/outer diameter of 0.8/1.2 mm was used as the nozzle. The nozzle motion was controlled via custom-written script functions and trajectory files. A volumetric rate in the range of 0.4–0.8 mL/min was used in most experiments, unless otherwise stated

After printing, the epoxy was cured at room temperature (\sim 24 °C) for 12–20 h inside the same bath. Desirable properties of epoxy resins are obtained by the reaction of the epoxy resin with a curing agent. The curing process directly depends on the type of the curing agent. The curing process is an exothermic reaction, and the generated heat has to be managed to prevent possible thermal degradation. Epikure curing agent 3234 cures at room temperature. After curing, the printed parts were readily retrieved from the bath. Cured parts were washed with running water until all the stuck bath on their surface was completely removed. Thermal post-curing was performed using an oven at 85 °C for 4 h.

Measurement of Rheological Properties. The rheological measurements were performed using an Anton Paar rheometer using a 50-mm upper cone with an angle of 0.5° and a 50 mm in diameter lower plate. Frequency sweeps were taken at 1% strain from 10² to 10⁻² Hz. The yield strength of the material was determined by applying a shear rate sweep from 10³ to 10⁻³ s⁻¹. A three-interval thixotropy test (3ITT) was performed to study the structural breakup and recovery characteristics of the support bath. This test has three steps. It can be performed in a controlled shear stress (CSS) mode or a controlled shear rate (CSR) mode. In the CSS mode, the shear stress or torque is preset on the rheometer, while in the CSR, the shear rate or rotational speed is preset on the rheometer. This test is performed at two different shear rates. The first and last steps are performed at low shear rates, while the second step is performed at a high shear rate. In this experiment, the time-dependent changes in the bath viscosity can be extracted. In the first interval, which is at a low shear rate, the goal is to obtain a constant viscosity to simulate the performance of the sample at rest or a no-shear condition. In the second interval, a high shear rate is exerted on the sample to simulate the fluid microstructure breakdown. The last step, which is similar to the first step, is performed at a low shear rate similar to the first interval to simulate how the fluid recovers after the high shear removal. In this work, a preshear of 0.1 s^{-1} was applied for 20 s. The low shear rate step was preset to 0.1 s^{-1} for 50 s followed by a high shear rate of 100 s⁻¹ for 10 s, and in the last interval, the shear rate was preset to 0.1 s⁻¹ for 100 s.

Calculation of the Rheological Properties of the Epoxy. The dynamic viscosity and density of the Epon resin are 25–45 P and 1174.3 kg/m³, and the dynamic viscosity and density of the curing agent TETA are 25 cP and 980 kg/m³, respectively. Note that the relation between dynamic viscosity (μ) and kinematic viscosity is $\nu = \frac{\mu}{\rho}$. Considering the dynamic viscosity, density (ρ), and mass fraction (x) of the Epon resin and the curing agent TETA, the viscosity of the epoxy was calculated using the Gambill equation ($\nu_E^{0.3} = \nu_R^{0.3} x_R + \nu_C^{0.3} x_C$). The calculated dynamic viscosity of the epoxy mixture was obtained to be 21.9 P.

Mechanical Characterization. The tensile tests were performed using a Lloyd LR5KPlus Universal Materials Testing Machine with a 500 N load cell. Each test was performed at room temperature at a 1 mm/min crosshead speed. Tensile specimens were punched out of the large 3D-printed sheets using an ASTM D638 Type V dogbone die at different directions with respect to the print direction. The cast samples were punched out from the cast sheets. Both sides of the samples were slightly polished before the tensile tests. Tensile specimens were gripped using Lloyd TG22 self-tightening roller grips.

At least three specimens for each direction were used to perform the tensile tests.

Statistical Analysis of the Mechanical Properties. To investigate the differences among the mechanical properties of the three groups of tensile tests for different printing layer directions, a statistical analysis was performed. One-way analysis of variance (ANOVA) was used for comparison of the mean value of two or more independent groups of samples. ANOVA tests whether the samples are drawn from populations with the same mean values or not. It calculates an F statistic, which is the ratio of the variance among the means of the groups to the variance within the samples. In the case that the group means are drawn from populations with the same mean values, the variance between the group means needs to be lower than the variance of the samples. Here, for mechanical properties of the three different layer directions (0, 45, and 90°), one-way ANOVA was performed. The P value corresponding to the F statistic of the oneway ANOVA was calculated to be 0.6, 0.12, 0.46, and 0.66 for the strength, modulus, strain to failure, and tensile toughness, respectively, which are higher than 0.05 (5% significance level). It means that, at this significance level, the mechanical properties of the 3D-printed specimens at different printing layer directions are not significantly different. Even though our data did not show any significant difference in the properties of the 3D-printed specimens in different printing layer directions, we proceeded to do a Tukey HSD (honestly significant differences) test to obtain more insight into the possible differences between each pair of data. The Tukey HSD test determines whether the relationship between two groups of data is statistically significant. The calculated Tukey HSD P values are presented in Table S3 and are higher than the significance level, demonstrating that there is no statistically significant difference in the mechanical properties of the tensile specimens prepared at different printing layer directions.

DSC/TGA Analysis. Differential scanning calorimetry (DSC) and thermal gravimetry analysis (TGA) were performed using an STA449/F5 Netzsch DSC/TGA. The sample size was limited between 12 and 14 mg. The measurements were performed from room temperatures up to 700 °C with a heating rate of 20 °C/min in a nitrogen gas environment.

SEM Imaging. A Zeiss Supra 40 SEM was utilized to measure the cross-sectional area of the printed filaments. Since a good electrical conductivity is required to obtain high-quality images, a gold—palladium film was sputtered on the epoxy parts. The composition of the epoxy was measured by the EDAX material analysis system.

Surface Finish Characterization. The surface finish of the printed samples was characterized using a Veeco Dektak 8 Profilometer. Surface height as a function of stylus scanning distance was recorded. The scanning rate was 6000 μ m in 225 s in the direction perpendicular to the printed layers.

Micro-CT Imaging. Micro-CT imaging was performed using a Nikon 225 kV C1 Granite based precision CT system. The voxel size in this equipment is up to 3 μ m. Micro-CT imaging was achieved by capturing the changes in attenuation of an X-ray beam through the sample. Cross-sectional images (2D slices) were then reconstructed from attenuation measurements by the detectors. These 2D slices were stacked on each other to create a 3D structure. The micro-CT data were processed using the Dragonfly software to produce 3D rendered models of the printed object and calculate the void fraction in the printed object.

■ ASSOCIATED CONTENT

Supporting Information

The Supporting Information is available free of charge at https://pubs.acs.org/doi/10.1021/acsami.0c19608.

Images of the printing details and 3D-printed epoxy structures (Figures S1–S5), tables of print duration and mechanical properties (Tables S1 and S2), statistical comparison of the elastic modulus, strain at break, and tensile toughness (Figure S6), results of the Tukey's

HSD test (Table S3), SEM images of printed structures (Figure S7, S9, and S19), references for the materials shown in Ashby plot (Table S4), schematic of printed filaments (Figure S8), nozzle speed (Table S5), comparison of experimentally measured filament diameter and the estimated diameter (Figure S10), loss and storage shear moduli vs frequency (Figure S11), measured bath viscosity and the calculated viscous force vs nozzle speed (Table S6), calculated Reynolds (Re) number (Figure S12), top-view and side-view optical images during 3D printing (Figure S13), 3ITT (Figure S14), DCS and TGA responses (Figures S15 and S16), measured mass vs time (Figure S17), EDS spectra (Figure S18), atomic percentage of the elements (Table S7), micro-CT images of the printed epoxy (Figure S20), and comparison of the epoxy viscosity with other common fluids (Figure S21) (PDF)

- 3D printing of thermosetting polymers (Movie S1) (MP4)
- 3D printing of an epoxy honeycomb structure (Movie S2) (MP4)
- 3D printing of an epoxy airfoil (Movie S3) (MP4)
- 3D printing of carbon fiber reinforced epoxy composite (Movie S4) (MP4)
- 3D printing of large epoxy sheets for tensile test specimens (Movie S5) (MP4)
- Movie shows crevasse formation within shallow depth in the bath (Movie S6) (MP4)

AUTHOR INFORMATION

Corresponding Author

Majid Minary-Jolandan — Department of Mechanical Engineering, University of Texas at Dallas, Richardson, Texas 75080, United States of America; orcid.org/0000-0003-2472-302X; Email: majid.minary@utdallas.edu

Authors

Mohammadreza Mahmoudi — Department of Mechanical Engineering, University of Texas at Dallas, Richardson, Texas 75080, United States of America

Scott R. Burlison — Department of Mechanical Engineering, University of Texas at Dallas, Richardson, Texas 75080, United States of America

Salvador Moreno – Department of Mechanical Engineering, University of Texas at Dallas, Richardson, Texas 75080, United States of America

Complete contact information is available at: https://pubs.acs.org/10.1021/acsami.0c19608

Author Contributions

M.M.J. and M.R.M. designed the research. M.R.M. conducted the majority of the experiments. M.M.J. and M.R.M. analyzed the data. S.R.B. and S.M. helped with the design of the printer, with G-codes for the prints, and in reviewing the manuscript.

Notes

The authors declare the following competing financial interest(s): A Provisional US patent has been submitted (serial number 63/041,364). The authors declare no other competing interests.

A provisional US patent has been submitted (serial number 63/041,364). The authors declare no other competing interests.

I

All the data are available upon request from the corresponding author.

ACKNOWLEDGMENTS

This work is supported by The Eugene McDermott Professorships at UT Dallas and partially through the National Science Foundation (CMMI, Award #1930621). The rheometer used in this work was acquired through NSF Grant CBET-1707063. We thank W. Voit's laboratory at UT Dallas for the ASTM standard die and Intron testing machine and Fatemeh Hassanipour's laboratory for the rheometer. We thank Runyu Zhang for acquiring the CT images and Se Oh and Yuxin Jaio for analysis of the CT images.

REFERENCES

- (1) Walker, D. A.; Hedrick, J. L.; Mirkin, C. A. Rapid, Large-Volume, Thermally Controlled 3D Printing Using a Mobile Liquid Interface. *Science* **2019**, *366*, 360.
- (2) Kelly, B. E.; Bhattacharya, I.; Heidari, H.; Shusteff, M.; Spadaccini, C. M.; Taylor, H. K. Volumetric Additive Manufacturing via Tomographic Reconstruction. *Science* **2019**, *363*, 1075–1079.
- (3) Truby, R. L.; Lewis, J. A. Printing Soft Matter in Three Dimensions. *Nature* **2016**, *540*, 371–378.
- (4) Tumbleston, J. R.; Shirvanyants, D.; Ermoshkin, N.; Janusziewicz, R.; Johnson, A. R.; Kelly, D.; Chen, K.; Pinschmidt, R.; Rolland, J. P.; Ermoshkin, A.; Samulski, E. T.; DeSimone, J. M. Continuous Liquid Interface Production of 3D Objects. *Science* **2015**, 347, 1349–1352.
- (5) de Beer, M. P.; van der Laan, H. L.; Cole, M. A.; Whelan, R. J.; Burns, M. A.; Scott, T. F. Rapid, Continuous Additive Manufacturing by Volumetric Polymerization Inhibition Patterning. *Sci. Adv.* **2019**, *S*, No. eaau8723.
- (6) Shusteff, M.; Browar, A. E. M.; Kelly, B. E.; Henriksson, J.; Weisgraber, T. H.; Panas, R. M.; Fang, N. X.; Spadaccini, C. M. One-Step Volumetric Additive Manufacturing of Complex Polymer Structures. *Sci. Adv.* **2017**, 3, No. eaao5496.
- (7) Kuang, X.; Wu, J.; Chen, K.; Zhao, Z.; Ding, Z.; Hu, F.; Fang, D.; Qi, H. J. Grayscale Digital Light Processing 3D Printing for Highly Functionally Graded Materials. Sci. Adv. 2019, 5, No. eaav5790.
- (8) Gantenbein, S.; Masania, K.; Woigk, W.; Sesseg, J. P. W.; Tervoort, T. A.; Studart, A. R. Three-dimensional Printing of Hierarchical Liquid-Crystal-Polymer Structures. *Nature* **2018**, *561*, 226–230.
- (9) Skylar-Scott, M. A.; Mueller, J.; Visser, C. W.; Lewis, J. A. Voxelated Soft Matter via Multimaterial Multinozzle 3D Printing. *Nature* **2019**, *575*, 330–335.
- (10) Robertson, I. D.; Yourdkhani, M.; Centellas, P. J.; Aw, J. E.; Ivanoff, D. G.; Goli, E.; Lloyd, E. M.; Dean, L. M.; Sottos, N. R.; Geubelle, P. H.; Moore, J. S.; White, S. R. Rapid Energy-Efficient Manufacturing of Polymers and Composites via Frontal Polymerization. *Nature* **2018**, *557*, 223–227.
- (11) Compton, B. G.; Lewis, J. A. 3D-Printing of Lightweight Cellular Composites. *Adv. Mater.* **2014**, *26*, 5930–5935.
- (12) Lind, J. U.; Busbee, T. A.; Valentine, A. D.; Pasqualini, F. S.; Yuan, H.; Yadid, M.; Park, S.-J.; Kotikian, A.; Nesmith, A. P.; Campbell, P. H.; Vlassak, J. J.; Lewis, J. A.; Parker, K. K. Instrumented Cardiac Microphysiological Devices via Multimaterial Three-dimensional Printing. *Nat. Mater.* **2017**, *16*, 303–308.
- (13) Mu, X.; Bertron, T.; Dunn, C.; Qiao, H.; Wu, J.; Zhao, Z.; Saldana, C.; Qi, H. J. Porous Polymeric Materials by 3D Printing of Photocurable Resin. *Mater. Horiz.* **2017**, *4*, 442–449.
- (14) Patel, D. K.; Sakhaei, A. H.; Layani, M.; Zhang, B.; Ge, Q.; Magdassi, S. Highly Stretchable and UV Curable Elastomers for Digital Light Processing Based 3D Printing. *Adv. Mater.* **2017**, 29, 1606000.

- (15) Zarek, M.; Layani, M.; Cooperstein, I.; Sachyani, E.; Cohn, D.; Magdassi, S. 3D Printing of Shape Memory Polymers for Flexible Electronic Devices. *Adv. Mater.* **2016**, *28*, 4449–4454.
- (16) Shi, Q.; Yu, K.; Kuang, X.; Mu, X.; Dunn, C. K.; Dunn, M. L.; Wang, T.; Jerry Qi, H. Recyclable 3D Printing of Vitrimer Epoxy. *Mater. Horiz.* **2017**, *4*, 598–607.
- (17) Pierson, H. A.; Celik, E.; Abbott, A.; De Jarnette, H.; Sierra Gutierrez, L.; Johnson, K.; Koerner, H.; Baur, J. W. Mechanical Properties of Printed Epoxy-Carbon Fiber Composites. *Experimental Mechanics* **2019**, *59*, 843–857.
- (18) Wu, W.; DeConinck, A.; Lewis, J. A. Omnidirectional Printing of 3D Microvascular Networks. *Adv. Mater.* **2011**, 23, H178–H183.
- (19) Bhattacharjee, T.; Zehnder, S. M.; Rowe, K. G.; Jain, S.; Nixon, R. M.; Sawyer, W. G.; Angelini, T. E. Writing in the Granular Gel Medium. *Sci. Adv.* **2015**, *1*, No. e1500655.
- (20) Hinton, T. J.; Jallerat, Q.; Palchesko, R. N.; Park, J. H.; Grodzicki, M. S.; Shue, H.-J.; Ramadan, M. H.; Hudson, A. R.; Feinberg, A. W. Three-dimensional Printing of Complex Biological Structures by Freeform Reversible Embedding of Suspended Hydrogels. *Sci. Adv.* **2015**, *1*, No. e1500758.
- (21) Hinton, T. J.; Hudson, A.; Pusch, K.; Lee, A.; Feinberg, A. W. 3D Printing PDMS Elastomer in a Hydrophilic Support Bath via Freeform Reversible Embedding. *ACS Biomater. Sci. Eng.* **2016**, *2*, 1781–1786.
- (22) O'Bryan, C. S.; Bhattacharjee, T.; Hart, S.; Kabb, C. P.; Schulze, K. D.; Chilakala, I.; Sumerlin, B. S.; Sawyer, W. G.; Angelini, T. E. Self-Assembled Micro-Organogels for 3D Printing Silicone Structures. *Sci. Adv.* **2017**, *3*, No. e1602800.
- (23) Afghah, F.; Altunbek, M.; Dikyol, C.; Koc, B. Preparation and Characterization of Nanoclay-Hydrogel Composite Support-Bath for Bioprinting of Complex structures. *Sci. Rep.* **2020**, *10*, 5257.
- (24) Yang, K.; Grant, J. C.; Lamey, P.; Joshi-Imre, A.; Lund, B. R.; Smaldone, R. A.; Voit, W. Diels—Alder Reversible Thermoset 3D Printing: Isotropic Thermoset Polymers via Fused Filament Fabrication. *Adv. Funct. Mater.* **2017**, 27, 1700318.
- (25) Nelson, A. Z.; Kundukad, B.; Wong, W. K.; Khan, S. A.; Doyle, P. S. Embedded Droplet Printing in Yield-Stress Fluids. *Proceedings of the National Academy of Sciences* **2020**, 117, 5671–5679.
- (26) Israelachvili, J. N., Unifying Concepts in Intermolecular and Interparticle Forces. In *Intermolecular and Surface Forces* (Third Edition), Israelachvili, J. N., Ed. Academic Press: San Diego, 2011; pp. 191–204.
- (27) Thom, A.; Taylor, G. I. The Flow Past Circular Cylinders at Low Speeds. *Proceedings of the Royal Society of London. Series A, Containing Papers of a Mathematical and Physical Character* **1933**, 141, 651–669.

Additive-Free and Support-Free 3D Printing of Thermosetting Polymers with Isotropic Mechanical Properties

Mohammadreza Mahmoudi, Scott R. Burlison, Salvador Moreno, and Majid Minary-Jolandan*

Department of Mechanical Engineering, University of Texas at Dallas, Richardson TX 75080, USA

* Corresponding author: majid.minary@utdallas.edu

This PDF file includes:

Supplementary text

Figures S1 to S21

Tables S1 to S7

Legends for Movies S1 to S6

SI References

Other supplementary materials for this manuscript include the following:

Movies S1 to S6

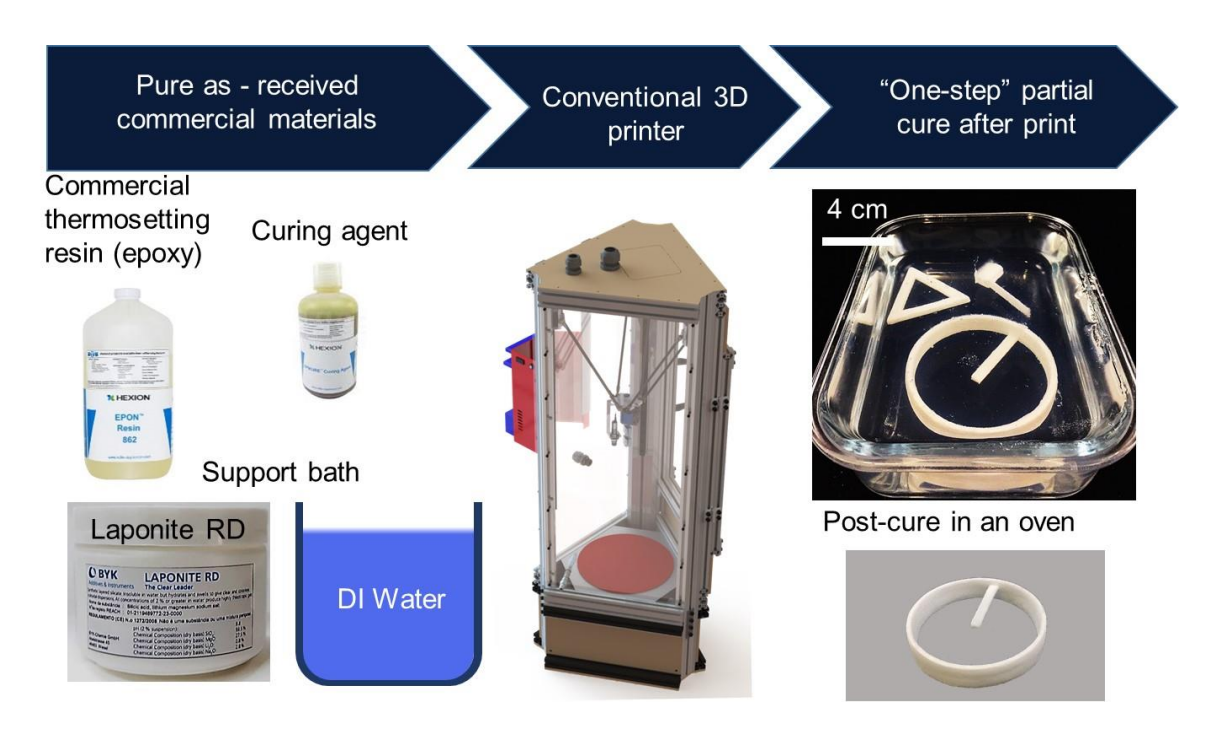


Figure S1 The process uses as-received commercial materials using conventional extrusion printers. The first partial curing is done in the same bath, followed by full curing in an oven.

Figure S2 shows a photo of a large container of the support bath. The bath preparation takes only a few hours and can be prepared in large containers for virtually any print size. One advantage of this support bath is its transparency, which facilitates monitoring the printing process in situ. Another advantage of the bath is its reusability, and the remaining portion of the bath can be remixed with water and Laponite to make a new bath. The bath costs < \$2/lit.



Figure S2 The bath is low-cost (<\$2/lit), easy and fast to prepare in large quantities, and it is transparent, which facilitates process monitoring.

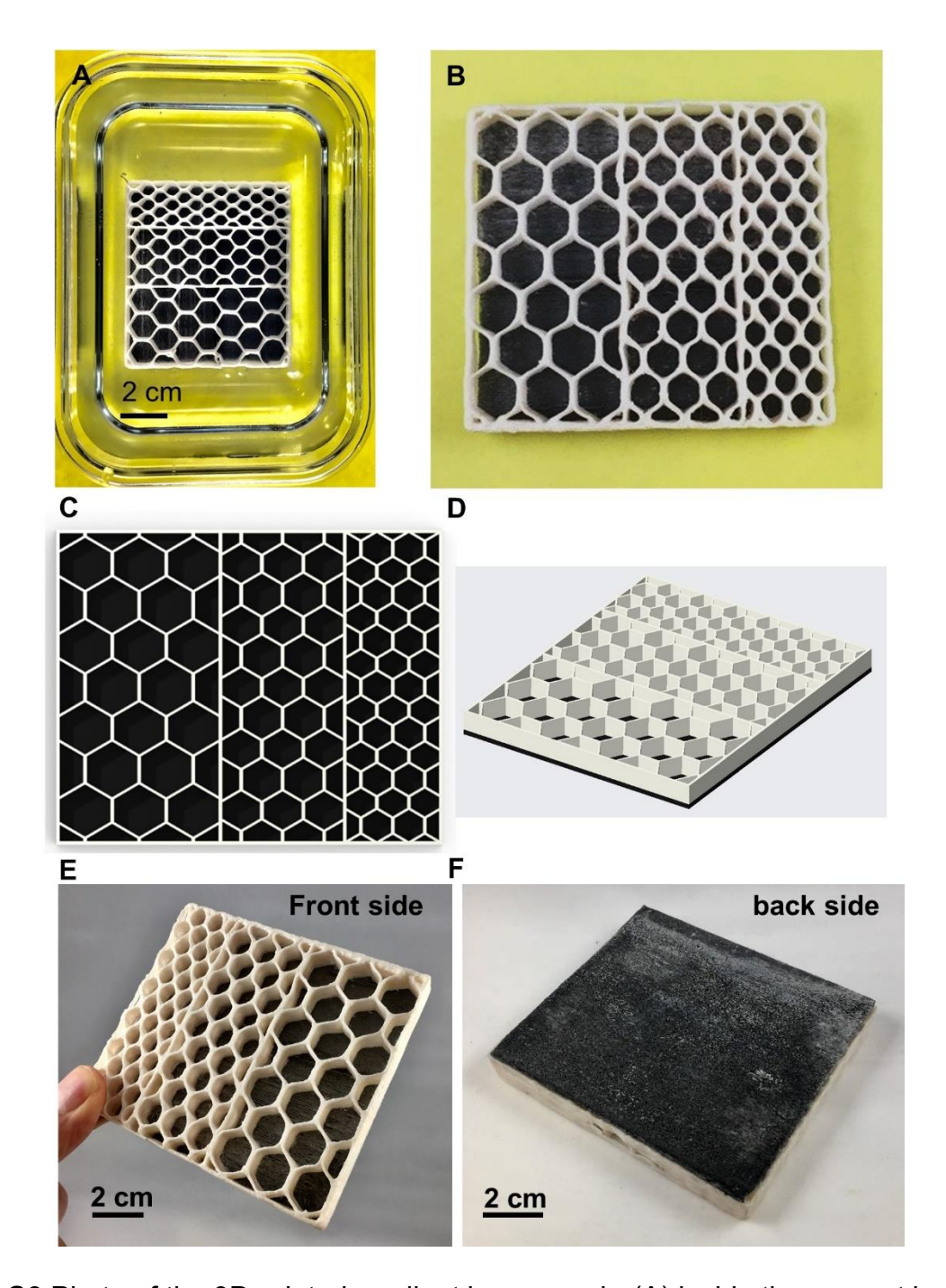


Figure S3 Photo of the 3D-printed gradient honeycomb, (A) inside the support bath after curing, and (B) after post-curing. (C) and (D) are the corresponding CAD files. (E) and (F) photos of the front-side and back-side that show the gradient structure, and the carbon-fiber-reinforced skin.

Table S1 Printing duration for various structures presented.

Geometry	Print duration (min)
Helix	0.4
Honeycomb	7.6
Gradient honeycomb	13
Propeller	7.3
Fan	10
Tensegrity table	14
Tensile test sheets	13.7
Airfoil	3

.

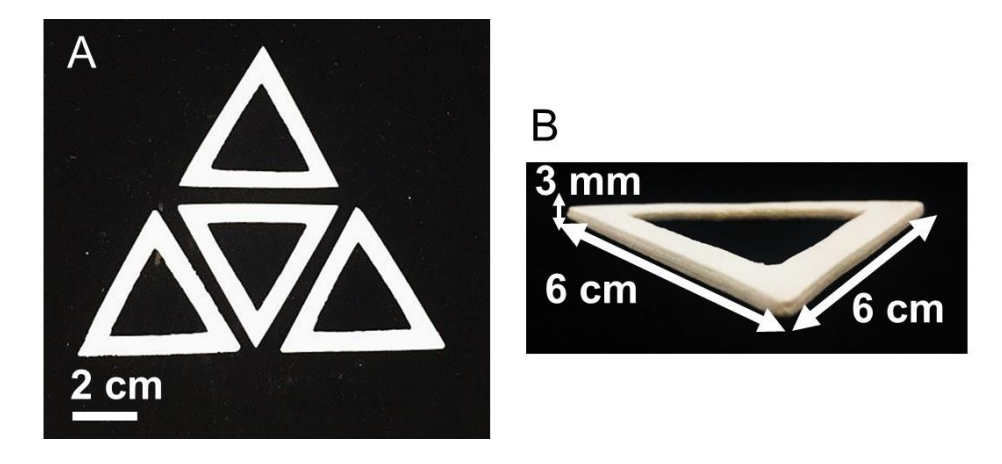


Figure S4 (A) Four 3D-printed equilateral triangles. (B) The iso-view of one triangle.

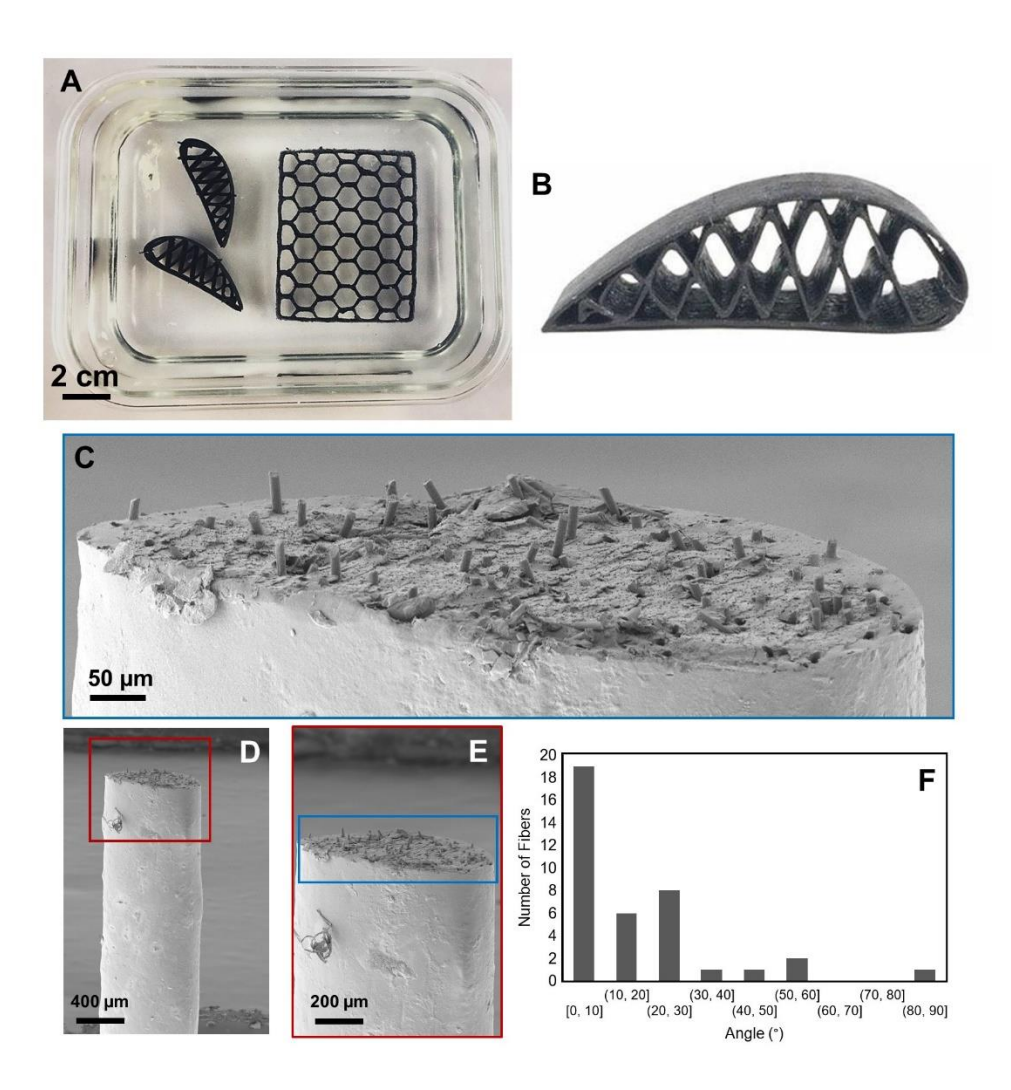


Figure S5 Chopped carbon fiber-reinforced epoxy parts, (A) after printing inside the support bath, (B) the airfoil after post-curing. (C) An SEM image of the cross-section 3D-printed of CF-reinforced epoxy. (C) - (E) SEM images of the carbon fiber-reinforced epoxy filament in different magnifications. (D) The histogram of the carbon fibers angles respect to the filament angle.

Table S2 Mechanical properties for the printed epoxy in different orientations with respect to the print direction.

Sample angle	le Strength (MPa) <i>E</i> (GPa) Strain at break (%		Strain at break (%)	Toughness (J/cm³)
0	40.1 ± 1.8	1.26 ± 0.1	3.7 ± 0.55	0.83 ± 0.09
45	35.3 ± 5	1.14 ± 0.05	4.0 ± 0.27	0.69 ± 0.17
90	37.5 ± 5.8	1.07 ± 0.08	4.3 ± 0.64	0.79 ± 0.18

Figure S6 Statistical comparison of the elastic modulus, strain at break, and tensile toughness for the printed epoxy in different orientations with respect to the print direction.

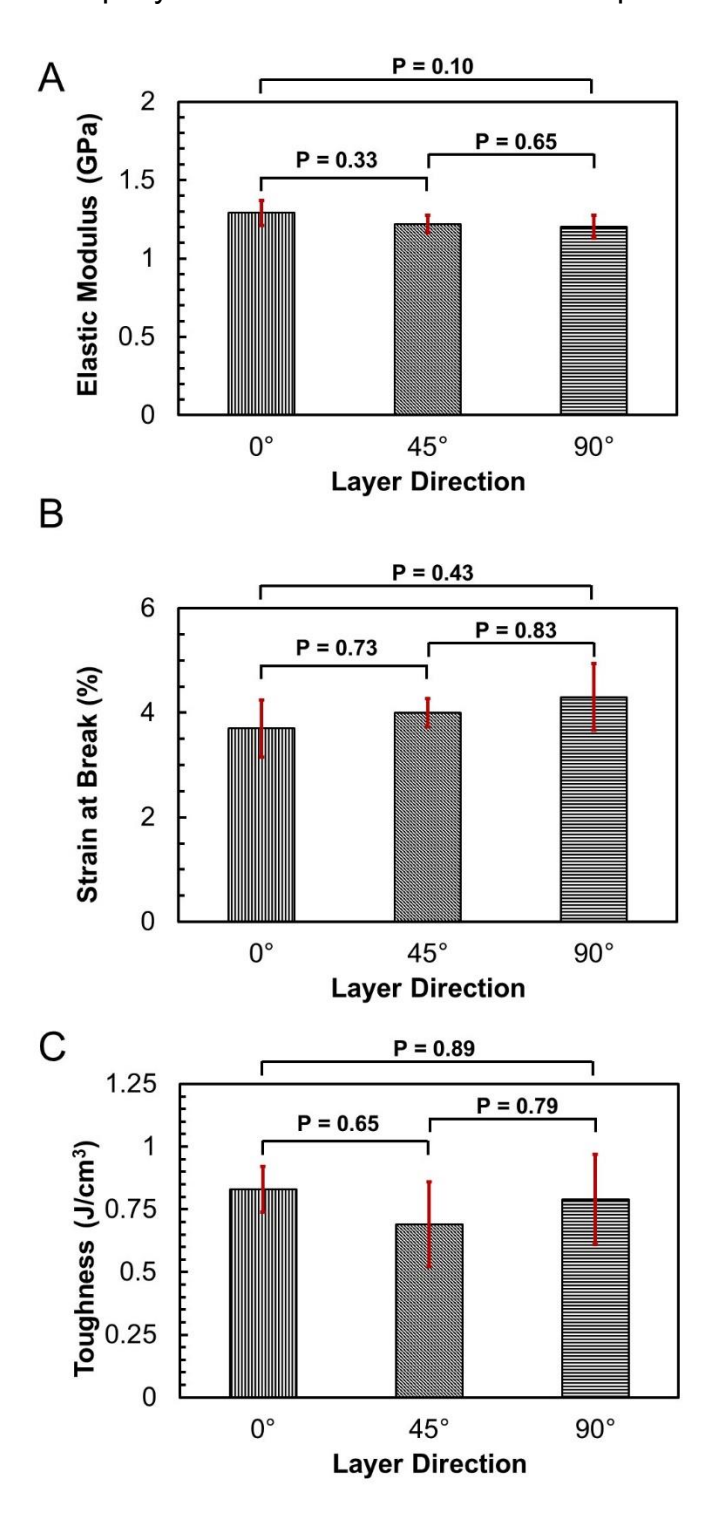


Table S3 The results of the Tukey's HSD test on tensile specimens with different print orientations. (A) strength, (B) elastic modulus, (C) strain at failure, and (D) tensile toughness.

В

D

Α	Printing Direction Pair	Tukey's HSD P-value	Tukey's HSD Inference
	0° vs 45°	0.57	Insignificant
	0° vs 90°	0.82	Insignificant
	45° vs 90°	0.88	Insignificant

Printing Direction Pair	Tukey's HSD P-value	Tukey's HSD Inference
0° vs 45°	0.33	Insignificant
0° vs 90°	0.10	Insignificant
45° vs 90°	0.65	Insignificant

C	Printing Direction Pair	Tukey's HSD P-value	Tukey's HSD Inference
	0° vs 45°	0.73	Insignificant
	0° vs 90°	0.43	Insignificant
	45° vs 90°	0.83	Insignificant

Printing Direction Pair	Tukey's HSD P-value	Tukey's HSD Inference
0° vs 45°	0.65	Insignificant
0° vs 90°	0.89	Insignificant
45° vs 90°	0.79	Insignificant

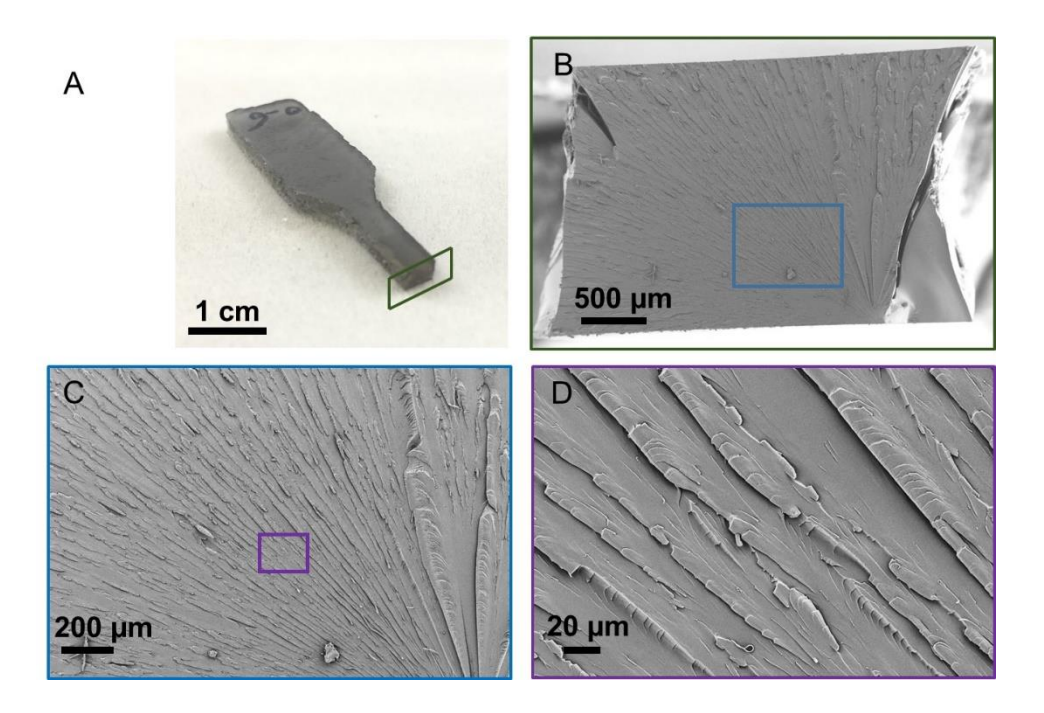


Figure S7 SEM images of the cross-section of the tensile specimen in various magnifications.

 Table S4 References for the materials shown in Ashby plot in Figure 2.

Material	Reference
Ероху	1
Epoxy-SiC	1
BPA Epoxy	2
Polyurethane Acrylate Resin	3
Vitrimer Epoxy	4
LCP	5
Spot-E Resin	6

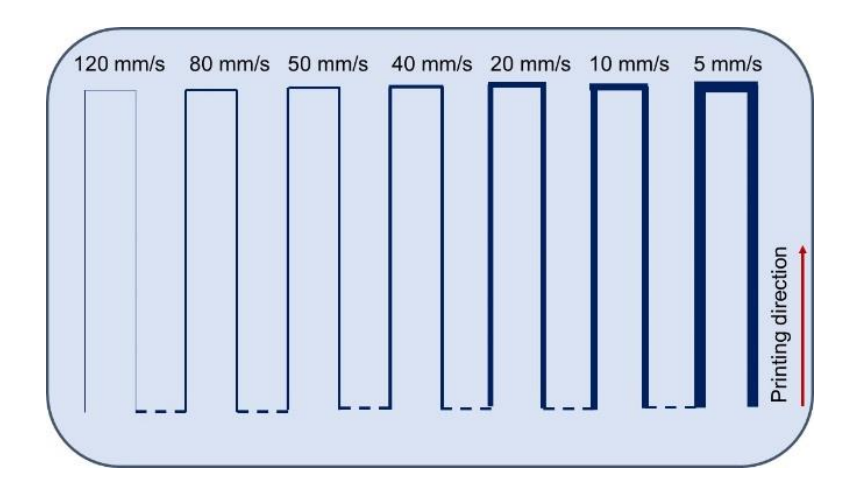


Figure S8 (A) The schematic of printed filaments at a constant flow rate and different nozzle speeds. The faster nozzle speeds result in thinner filaments.

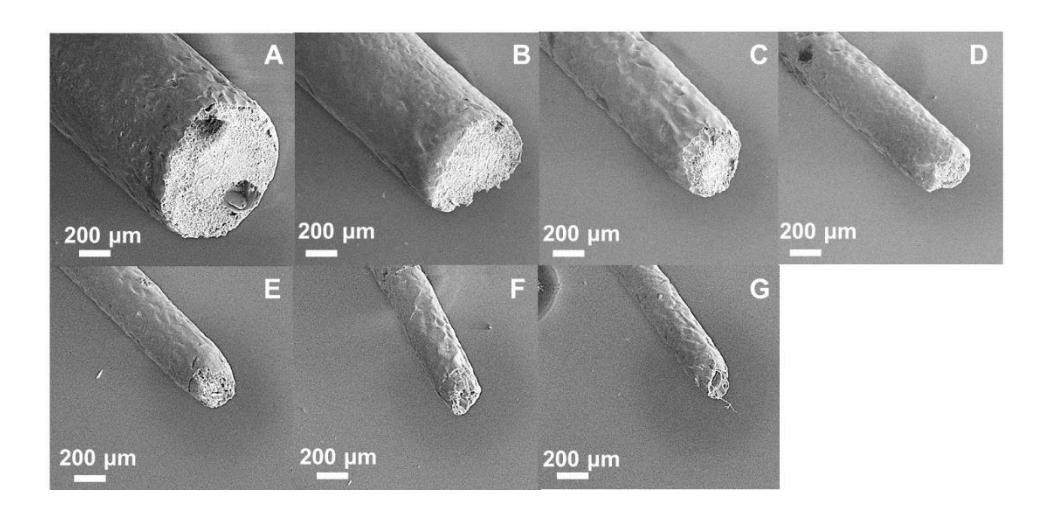


Figure S9 The SEM images of printed filaments at various speeds given in Table S5.

Table S5 The nozzle speed corresponding to SEM images in S9.

Sample	Nozzle speed (mm/s)	Diameter (μm)
Α	5	945.2
В	10	638.4
С	20	437
D	40	344.5
Е	50	322.4
F	80	257.8
G	120	219.2

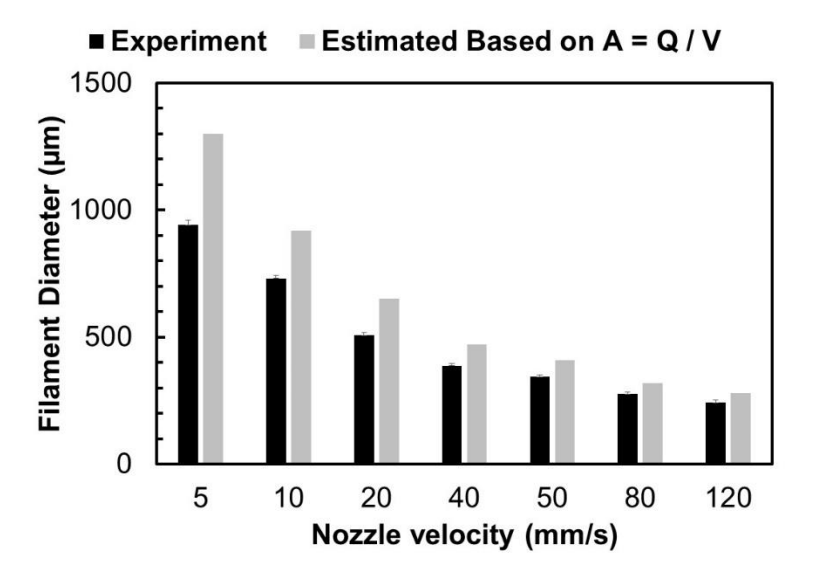


Figure S10 Comparison of experimentally measured filament diameter and the estimated diameter calculated from Q/V vs. nozzle speed.

Figure S11 shows the modulus versus frequency for the support bath. The storage modulus (G') is related to the elasticity of the support bath whereas the loss modulus (G'') is related to the viscous behavior. The storage modulus is greater than the loss modulus in the frequency range of 0.01 Hz - 100 Hz. This is the predominant characteristic in viscoelastic solids.

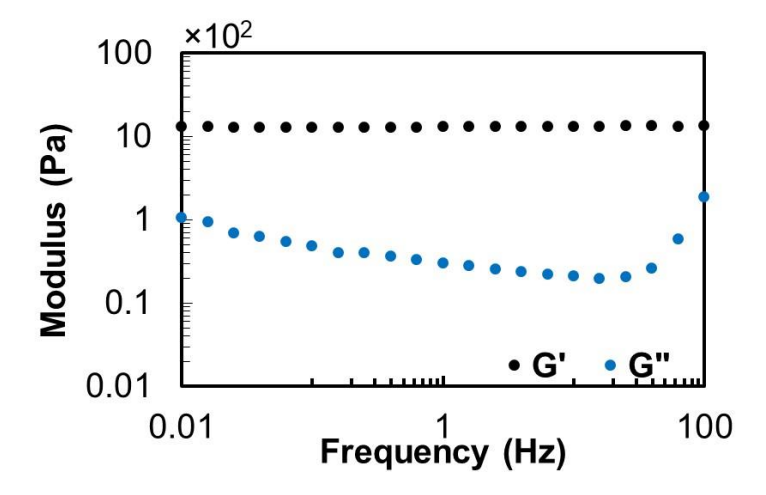


Figure S11 The loss and storage shear moduli vs. frequency for the bath.

Table S6 The measured bath viscosity and the calculated viscous force vs. nozzle speed.

Nozzle velocity V [mm/s]	Shear strain rate $\dot{\gamma}pproxrac{v}{d}$ [1/s]	Bath viscosity η [Pa.s]	Viscous force $\frac{V.\eta}{d}$ [Pa]
5	4.17	11.83	49.29
10	8.33	6.03	50.25
20	16.67	3.06	51
40	33.33	1.49	49.67
50	41.67	1.25	52.08
80	66.67	0.78	52
120	100	0.52	52

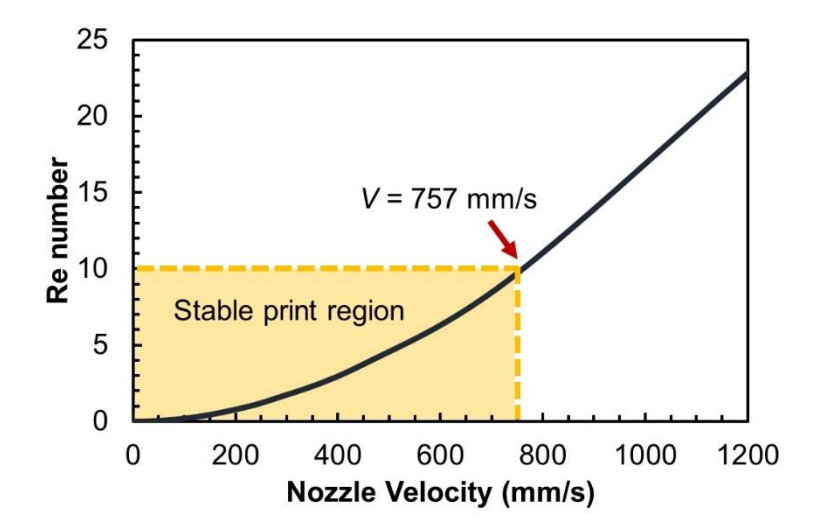


Figure S12 The calculated Reynolds (Re) number for the bath vs. the nozzle speed. At nozzle speed of V = 757 mm/s, Re = 10, which could be the onset of turbulent flow in the bath resulting in recirculating flow and unstable printing. The bath Re was calculated form the experimentally measured bath viscosity vs. the nozzle velocity.

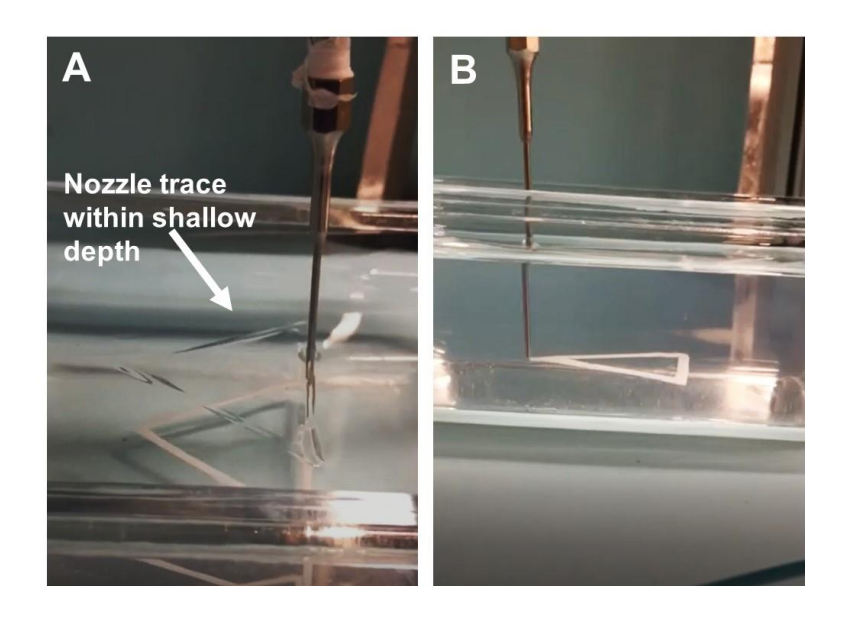


Figure S13 (A) and (B) top-view and side-view optical images during 3D printing. The nozzle trace can be observed in the top-view image for shallow depth, while no trace is observed for deeper depth.

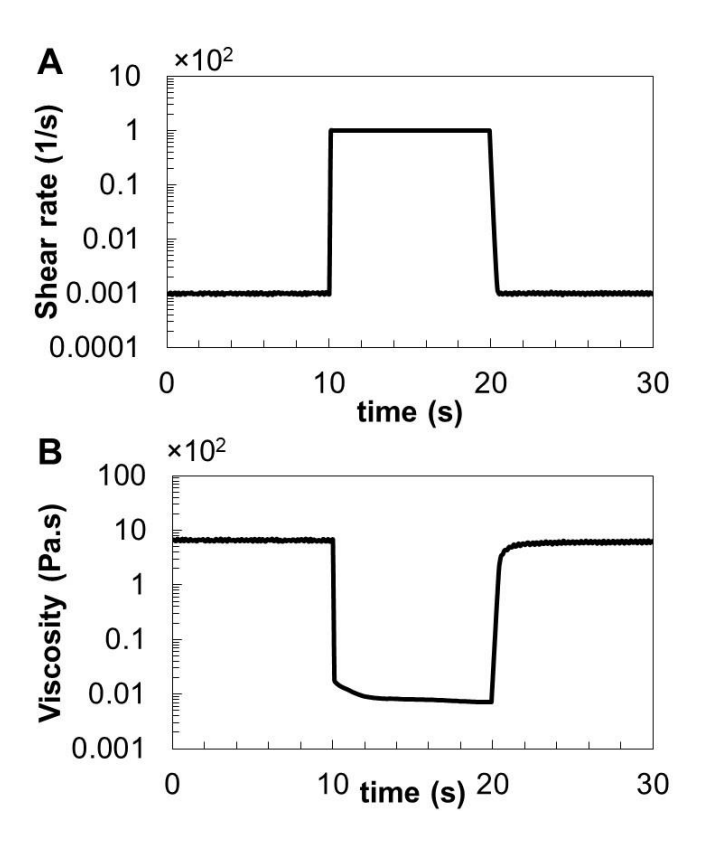


Figure S14 The 3ITT test, (A) shear rate versus time, (B) viscosity versus time.

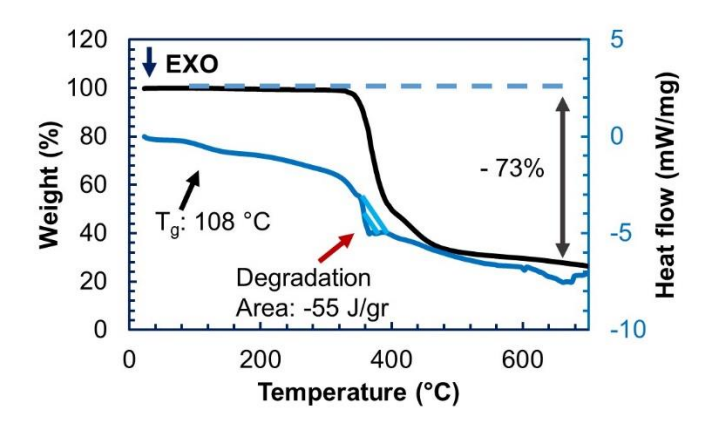


Figure S15 The DSC/TGA responses of the cast epoxy.

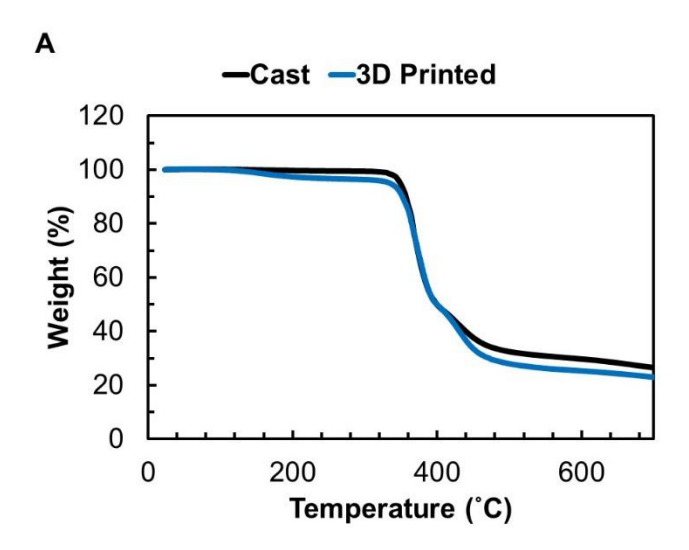


Figure S16 The TGA responses of the cast and 3D-printed epoxy.

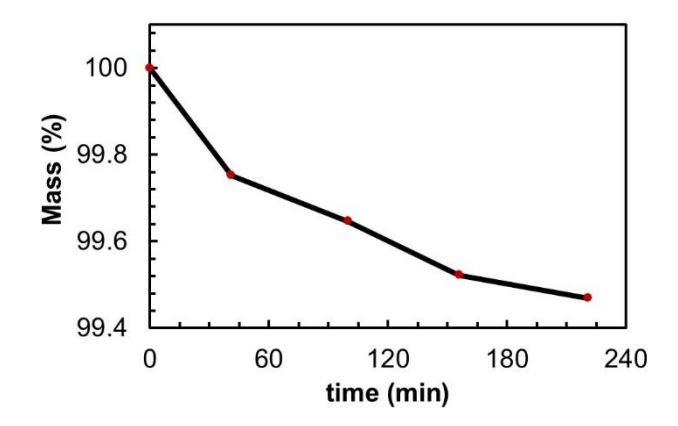


Figure S17 Measured mass vs. time for the partially cured epoxy indicates negligible water evaporation from the sample.

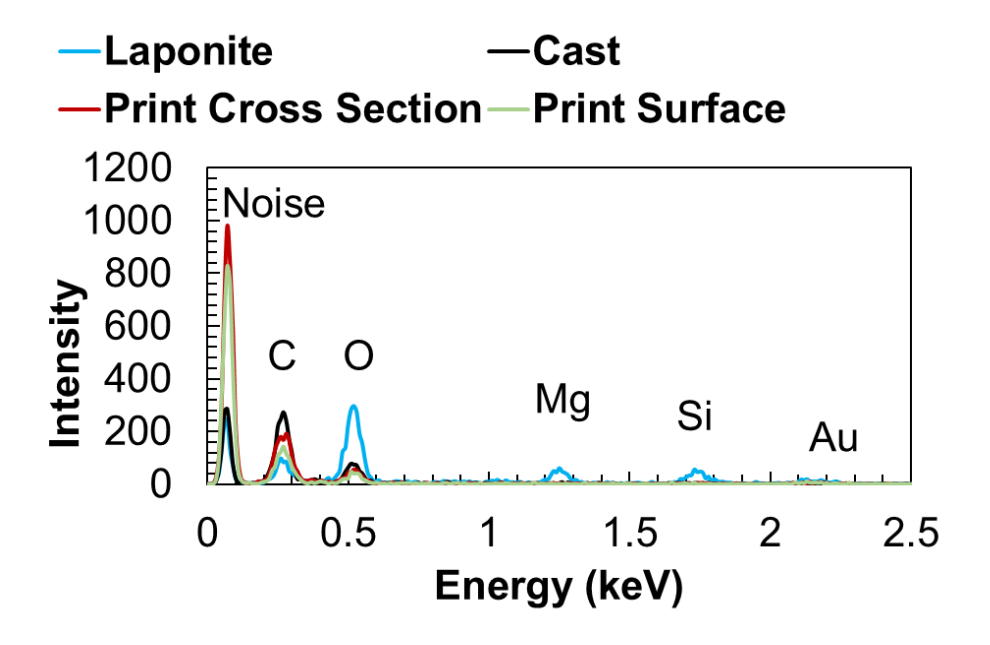


Figure S18 The EDS spectra of the Laponite, cast epoxy, cross-section and surface of the printed epoxy.

Table S7 The atomic percentage of the elements from the EDS spectra in S18.

Element (at. %)	С	0	Mg	Si	Au
Cast	87.18	12.82	0	0	0
Print surface	86.77	13.23	0	0	0
Print cross-section	88.5	11.5	0	0	0
Laponite	40.71	45.75	5.48	7.01	1.06

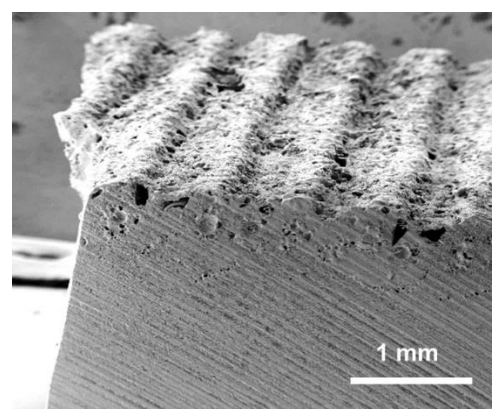


Figure S19 An SEM image of the printed epoxy sheet used for tensile test. This sample was cut using a diamond saw from the printed sheet, and the lines on the side-surface are traces of the saw. The top surface shows the as-print (unpolished) surface of the sheet.

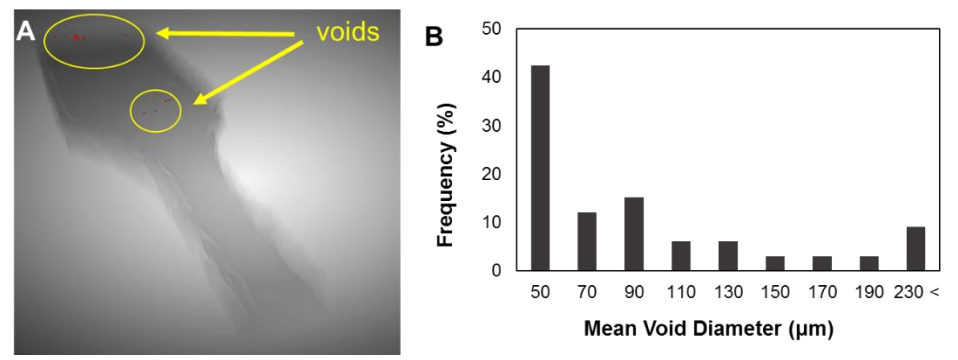


Figure S20 (A) A 3D micro-CT image of a broken tensile specimen. The red dots are identified as voids. (B) The void diameter distribution histogram.

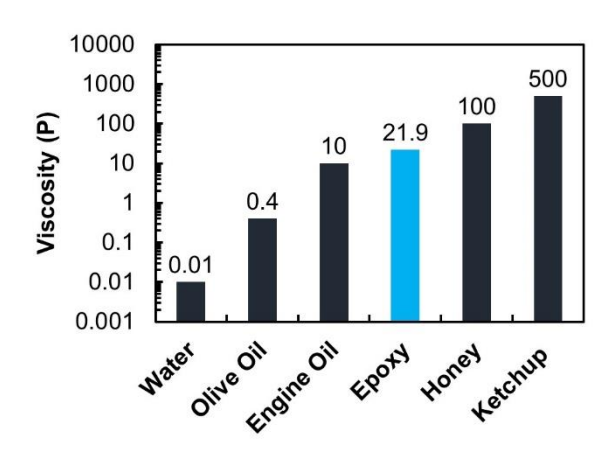


Figure S21 The comparison of the epoxy viscosity with other common fluids. (10 P = 1 Pa.s).

Movie S1 (separate file). 3D-printing of thermosetting polymers

Movie S2 (separate file). 3D-printing of an epoxy honeycomb structure

Movie S3 (separate file). 3D-printing of an epoxy airfoil

Movie S4 (separate file). 3D-printing of carbon fiber-reinforced epoxy composite

Movie S5 (separate file). 3D-printing of large epoxy sheets for tensile test specimens

Movie S6 (separate file). Movie shows crevasse formation within shallow dept in the bath

SI References

- 1. Compton, B. G.; Lewis, J. A., 3D-printing of lightweight cellular composites. *Advanced materials* **2014**, *26* (34), 5930-5.
- 2. Robertson, I. D.; Yourdkhani, M.; Centellas, P. J.; Aw, J. E.; Ivanoff, D. G.; Goli, E.; Lloyd, E. M.; Dean, L. M.; Sottos, N. R.; Geubelle, P. H.; Moore, J. S.; White, S. R., Rapid energy-efficient manufacturing of polymers and composites via frontal polymerization. *Nature* **2018**, *557* (7704), 223-227.
- 3. Walker, D. A.; Hedrick, J. L.; Mirkin, C. A., Rapid, large-volume, thermally controlled 3D printing using a mobile liquid interface. *Science* **2019**, *366* (6463), 360-+.
- 4. Shi, Q.; Yu, K.; Kuang, X.; Mu, X. M.; Dunn, C. K.; Dunn, M. L.; Wang, T. J.; Qi, H. J., Recyclable 3D Printing of Vitrimer Epoxy. *Materials Horizons* **2017**, *4* (4), 598-607.
- 5. Gantenbein, S.; Masania, K.; Woigk, W.; Sesseg, J. P. W.; Tervoort, T. A.; Studart, A. R., Three-dimensional Printing of Hierarchical Liquid-Crystal-Polymer Structures. *Nature* **2018**, *561* (7722), 226-230.
- 6. Mu, X.; Bertron, T.; Dunn, C.; Qiao, H.; Wu, J.; Zhao, Z.; Saldana, C.; Qi, H. J., Porous Polymeric Materials by 3D Printing of Photocurable Resin. *Materials Horizons* **2017**, *4* (3), 442-449.